Using Dark Fiber and Distributed Acoustic Sensing to Characterize a Geothermal System in the Imperial Valley, Southern California

Feng Cheng[1], Jonathan B Ajo-Franklin[2], Avinash Nayak[3], Veronica Rodriguez Tribaldos[3], Robert Mellors[4], and Patrick Dobson[3]

[1]Zhejiang University,Rice University
[2]Rice University
[3]Lawrence Berkeley National Laboratory
[4]Scripps Institution of Oceanography

November 21, 2022

Abstract

The Imperial Valley, CA, is a tectonically active transtensional basin located south of the Salton Sea; the area hosts numerous geothermal fields, including significant hidden hydrothermal resources without surface manifestations. Development of inexpensive, rugged, and highly-sensitive exploration techniques for undiscovered geothermal systems is critical for accelerating geothermal power deployment as well as unlocking a low-carbon energy future. We present a case study utilizing distributed acoustic sensing (DAS) and ambient noise interferometry for geothermal reservoir imaging utilizing an unlit fiber-optic telecommunication infrastructure (dark fiber). The study utilizes passive DAS data acquired from early November 2020 over a ~28-kilometer section of fiber from Calipatria, CA to Imperial, CA. We apply ambient noise interferometry to retrieve coherent signals from DAS records, and develop a spatial stacking technique to attenuate effects from persistent localized noise sources and to enhance retrieval of coherent surface waves. As a result, we are able to obtain high-resolution two-dimensional (2D) S wave velocity (Vs) structure to 3 km depth based on joint inversion of both the fundamental and higher overtones. We observe a previously unmapped high Vs and low Vp/Vs ratio feature beneath the Brawley geothermal system that we interpret to be a zone of hydrothermal mineralization and lower porosity. This interpretation is consistent with a host of other measurements including surface heat flow, gravity anomalies, and available borehole wireline data. These results demonstrate the potential utility of DAS deployed on dark fiber for geothermal system exploration and characterization in the appropriate contexts.

Using Dark Fiber and Distributed Acoustic Sensing to Characterize a Geothermal System in the Imperial Valley, Southern California

Feng Cheng[1,2], Jonathan B. Ajo-Franklin[2,3,*], Avinash Nayak[3], Veronica Rodriguez Tribaldos[3], Robert Mellors[4], Patrick Dobson[3], and the Imperial Valley Dark Fiber Team

[1]School of Earth Sciences, Zhejiang University, 38 Zheda Rd., Hangzhou, Zhejiang 310027, China
[2]Dept. of Earth, Environmental, and Planetary Sciences, Rice University, 6100 Main St., Houston, TX 77005, USA
[3]Lawrence Berkeley National Laboratory, 1 Cyclotron Rd., Berkeley, CA 94720, USA
[4]Institute of Geophysics and Planetary Physics, Scripps Institution of Oceanography, UC San Diego, La Jolla, CA 92037, USA

Key Points:

- We utilize high-resolution ambient noise imaging to characterize a geothermal system using DAS and dark fiber.
- We develop a spatial stacking technique to attenuate the effects of persistent local noise sources and enhance the retrieved EGF.
- We image a zone of high shear wave velocity beneath the Brawley geothermal field, which we interpret to be a zone of hydrothermal alteration.

Corresponding author: Jonathan B. Ajo-Franklin, `ja62@rice.edu`

Abstract

The Imperial Valley, CA, is a tectonically active transtensional basin located south of the Salton Sea; the area hosts numerous geothermal fields, including significant hidden hydrothermal resources without surface manifestations. Development of inexpensive, rugged, and highly-sensitive exploration techniques for undiscovered geothermal systems is critical for accelerating geothermal power deployment as well as unlocking a low-carbon energy future. We present a case study utilizing distributed acoustic sensing (DAS) and ambient noise interferometry for geothermal reservoir imaging utilizing an unlit fiber-optic telecommunication infrastructure (dark fiber). The study utilizes passive DAS data acquired from early November 2020 over a ∼28-kilometer section of fiber from Calipatria, CA to Imperial, CA. We apply ambient noise interferometry to retrieve coherent signals from DAS records, and develop a spatial stacking technique to attenuate effects from persistent localized noise sources and to enhance retrieval of coherent surface waves. As a result, we are able to obtain high-resolution two-dimensional (2D) S wave velocity (V_s) structure to 3 km depth based on joint inversion of both the fundamental and higher overtones. We observe a previously unmapped high V_s and low V_p/V_s ratio feature beneath the Brawley geothermal system that we interpret to be a zone of hydrothermal mineralization and lower porosity. This interpretation is consistent with a host of other measurements including surface heat flow, gravity anomalies, and available borehole wireline data. These results demonstrate the potential utility of DAS deployed on dark fiber for geothermal system exploration and characterization in the appropriate contexts.

Plain Language Summary

Geothermal resources are considered a valuable component of our transition to a zero-emissions sustainable energy future; the undiscovered geothermal energy potential beneath our feet is vast. In the Imperial Valley, CA, three of the four producing geothermal fields have no active surface features. Development of inexpensive, rugged, and highly-sensitive exploration techniques for undiscovered geothermal systems is a critical step in accelerating geothermal power deployment. We utilize a ∼28-kilometer section of existing unused telecommunication fiber as seismic sensors (called distributed acoustic sensing, DAS) to characterize the subsurface geothermal resources. Our results reveal significant high-velocity anomalies beneath the Brawley Geothermal Field area; these are coincident with observations from boreholes, heat flow and gravity surveys which indicate hydrothermal alteration has a pronounced effect on the physical properties of the sediments.

1 Introduction

Geothermal energy is considered a key base-load resource for transitioning to a zero-emissions sustainable energy future (Sbrana et al., 2021). Geothermal energy currently accounts for 0.4% of net electricity generation in the United States (EIA, 2021). According to a recent National Renewable Energy Lab report, U.S. geothermal net summer capacity could increase from 2.5 to 6 GigaWatts (GW) by 2050 (Robins et al., 2021). In 2008, the U.S. Geological Survey (USGS) released summary results of an assessment of the electric power production potential from the moderate- and high-temperature geothermal resources of the United States, and indicated the estimated mean power production potential from undiscovered geothermal resources is more than three times the estimated mean potential from identified geothermal systems (Williams et al., 2008). A significant portion (∼30%) of the estimated undiscovered resource in the US is predicted to occur within the Imperial Valley (Williams et al., 2009). Development of improved exploration strategies for undiscovered geothermal systems is critical for accelerating geothermal power deployment (Williams et al., 2009; Dobson, 2016).

Active hydrothermal systems are often associated with measurable differences in physical properties (e.g., high heat flow, low electrical resistivity, elevated density, and attenuation of high frequency elastic waves). As a result, geophysical methods play a key role in geothermal reservoir exploration (e.g., Combs, 1978; Flóvenz & Saemundsson, 1993; Thanassoulas, 1991; Santos & Rivas, 2009; Zucca et al., 1994). For example, heat flow anomalies, derived from temperature measurements in shallow boreholes, can be used to locate and outline potential geothermal fields (Fahnestock et al., 2001; Burton-Johnson et al., 2020). Gravity surveys can be used to study the depth of fill in intermontaine valleys, locate intrusive masses of rock and delineate geothermal features (Atef et al., 2016; Guglielmetti & Moscariello, 2021). A combination of resistivity studies, derived from active or passive electromagnetic (EM) surveys, and heat flow measurements from temperature gradient wells are often used to search for zones likely to host permeable geothermal reservoirs sealed with an overlying clay cap (Anderson et al., 2000; Munoz, 2014; Gao et al., 2018). Seismic reflection profiles can be used to identify faults, which may facilitate flow, in hot sedimentary systems using reflection offsets, as well as image basement contacts and verify structures related to tectonic processes relevant to geothermal system development (Brogi et al., 2005; Lüschen et al., 2011; McGuire et al., 2015). Lastly, microseismic surveys are widely used for studying slip on seismogenic faults which may preserve permeability (Ward, 1972; Combs & Hadley, 1977; Lellouch et al., 2020). However, considering the limitations of these different approaches, suites of methods are typically used to verify proposed system location, conditions, and associated structures before exploratory wells are drilled (Soyer et al., 2018; Ars et al., 2019).

Compared to relatively expensive active-source seismic methods, ambient noise interferometry can be a cost-effective imaging approach, valuable for both characterization and long-term monitoring. Following the pioneering work of Campillo and Paul (2003), ambient noise interferometry can be used to estimate an empirical Green's function (EGF) between two receivers by cross-correlating the ambient seismic wave field (Shapiro & Campillo, 2004; Snieder, 2004; Wapenaar, 2004; Bensen et al., 2007; Snieder et al., 2009; Nakata et al., 2015; Cheng et al., 2016, 2018; Behm et al., 2019; Fichtner et al., 2020). In recent years, ambient noise interferometry techniques have found a variety of applications for geothermal reservoir imaging by using dense nodal arrays (e.g., Lehujeur et al., 2018; Spica et al., 2018; Martins et al., 2019, 2020; Planès et al., 2020; Zhou et al., 2021; Cheng et al., 2021a). Recorded EGFs are often rich in surface wave energy, hence the most commonly retrieved physical property from ambient noise studies are shear wave velocities estimated using surface wave tomography methods.

Currently, there are still large portions of western basins of the U.S. that are relevant to geothermal energy production but poorly mapped using classical high-resolution seismic methods. This is due to the high costs of active seismic surveys and the lack of availability of Large-N passive seismic datasets required for ambient noise imaging. These factors likely result in both missed prospects as well as limitations in our understanding of regional geological frameworks relevant to geothermal prospecting.

Distributed fiber optic sensing is a family of techniques that utilizes standard optical fibers to make measurements of local physical parameters including temperature (Tyler et al., 2009), static strain (Masoudi & Newson, 2016), and most recently low amplitude dynamic strain or strain rate (Lindsey & Martin, 2021). The last approach, referred to as distributed acoustic sensing (DAS), is an emerging technology that repurposes a fiber-optic cable as a dense array of seismic sensors and in some environments is transforming seismic acquisition (Daley et al., 2013; Dou et al., 2017; Lindsey et al., 2017; Ajo-Franklin et al., 2019; Zhan, 2020; Martin et al., 2021; Cheng et al., 2021b, 2022). DAS utilizes short pulses of laser light to interferometrically measure minute extensional strains (or strain rates) over spatially continuous intervals along an optical fiber (Hartog, 2017) with spatial resolutions down to the meter scale, linear extents from 10s to 100s of km, and bandwidth from the kHz range to quasi-static depending on interrogator unit and measurement parameters (Lindsey et al., 2020; Paitz et al., 2021). The ability to plug an interrogator unit into existing unused telecommunications fiber has enabled easy access to urban locations where traditional seismic acquisition systems would be prohibitively difficult or costly to deploy (Lindsey & Martin, 2021). Recently, several DAS-related feasibility studies have been conducted to characterize geothermal reservoirs (e.g., Feigl & Team, 2017; Feigl & Parker, 2019; Chalari et al., 2019; Kasahara et al., 2020; Schölderle et al., 2021; Lellouch et al., 2021; Chang & Nakata, 2022).

In the Imperial Valley, CA, there are three producing geothermal systems that have no active surface thermal features, and there are likely additional undiscovered resources. In this study we investigate the potential of high-resolution ambient noise imaging, using DAS data acquired on existing unused telecommunications fiber, to image geothermal reservoir structure. We present the acquisition and the main characteristics of the ambient seismic noise records obtained from a ∼28-km DAS array that runs along a portion of Imperial Valley, CA, and crosses the producing Brawley geothermal field. We extract high quality Rayleigh waves based on ambient noise interferometry, and apply surface wave inversion across the profile to generate a two-dimensional (2-D) S wave velocity model. The resulting image identifies a zone of high V_s closely correlated with the Brawley heat flow anomaly; we hypothesize that the imaged feature is due to a zone of hydrothermal mineralization at the core of the Brawley geothermal field, which results in significant reduction in porosity. We conclude by attempting to verify this hypothesis using secondary datasets including regional velocity models, existing wireline logs, gravity measurements, and heat flow data. Our results demonstrate the feasibility of such passive DAS surveys for detecting and characterizing structure relevant to geothermal systems at the basin scale.

2 Area and Data

The Imperial Valley, south of the Salton sea, is part of the landward extension of the Gulf of California, within a broad, structural trough (Salton Trough) partly filled with deltaic silts, sands and gravels of late Tertiary age, capped by Quaternary alluvium and lake sediments (Jackson, 1981). The Salton Trough is a tectonically active sedimentary pull-apart basin located at the southern tip of the San Andreas Fault system as it steps over into the continental transitional zone on the boundary between the North American Plate and the Pacific Plate (Kaspereit et al., 2016). The transition from the transform faulting of the San Andreas Fault system to the rifting associated with the East Pacific Rise, results in a series of smaller scale pull-apart basins of different sizes that connect right-stepping, strike-slip faults that strike generally northwest (Elders et al., 1972; Hill et al., 1975; Johnson & Hadley, 1976; Hill, 1977; Fuis et al., 1982). This pattern of faulting forms in transtensional shear zones where there are structures related to both strike-slip and extension. Major faults (red lines in Figure 1a) in the region include the Imperial Fault (IF), the Superstition Hills Fault (SHF), the Superstition Mountain Fault (SMF) and the Brawley Fault (BF, we use the Brawley fault as mapped by Hill et al. (1975); Jackson (1981)). The southeast end of the San Andreas Fault is linked to the northwest end of the Imperial Fault by a band of seismicity referred to as the Brawley Seismic Zone (BSZ, outlined by the orange line in Figure 1a). Within the trough, all these tectonic forces are currently active and allow mantle-derived magmas to intrude into the sedimentary sequence. The existence of igneous intrusive bodies is inferred from gravity and magnetic anomalies, high seismic velocities, and a localized temperature anomaly, all of which are coincident with the Quaternary volcanic domes along the southern shore of the Salton Sea (Biehler, 1964; Larson et al., 1968; Lomnitz et al., 1970; Elders et al., 1972). The magmatic intrusions serve as heat sources to drive hydrothermal systems and alter the thermal structure of the sediments with the associated hydrothermal alteration, causing changes in the dominant mineral assemblages (McGuire et al., 2015).

The Salton Trough is filled with late Tertiary and Quaternary clastic and evaporitic sediments. The sedimentary fill consists primarily of Pliocene to Holocene deltaic deposits derived from the Colorado River with coarser detritus along the margins derived from the adjacent mountain ranges (Muffler & White, 1969; Winker, 1987). The thick sediments contain geothermal brines near the known geothermal resource areas (KGRA) (highlighted with green polygons in Figure 1a): Salton Sea Geothermal Field (SSGF), Brawley Geothermal Field (BGF), East Mesa Geothermal Field (EMGF) and Heber Geothermal Field (HGF); there are additional KGRAs in the area (such as Westmorland, Glamis, and Dunes) that have yet to be developed.

Local seismicity and earthquake focal mechanisms across the area have been studied (Hill et al., 1975; Marone et al., 1991; Lin et al., 2007; Lohman & McGuire, 2007; Brodsky & Lajoie, 2013; Hauksson et al., 2013). The seismicity was characterized by narrow zones of right lateral events extending between the Brawley and the Imperial faults within the BSZ, and a broader zone of right lateral activity along the San Jacinto Fault. Seismic activity was also observed at the Salton Sea and Brawley geothermal fields, which lie on the Brawley fault, and at the Heber geothermal field near the extension of the San Jacinto Fault. In contrast, the Glamis, Dunes and East Mesa fields have had low levels of historical seismicity. These observations are consistent with the historical earthquake catalog (green-to-blue scatters in Figure 1a) relocated by Hauksson et al. (2012).

As part of the USGS regional assessment of unidentified geothermal systems in the Imperial Valley, a regional heat flow map was generated (Williams et al., 2007, 2008). Figure 1b clearly shows that the SSGF geothermal system and three previously hidden geothermal systems (BGF, EMGF, and HGF), highlighted with green polygons, are all associated with regions of elevated heat flow. For example, the heat flow reaches 350 mW/m^2 near the BGF. The average heat flow in the region is roughly twice the national average (Lachenbruch & Sass, 1973). The heat flow map also shows a number of other areas with elevated heat flow values, suggesting that there might be significant thermal resources in the Imperial Valley area that are yet to be discovered and developed (Williams et al., 2007, 2008; Dobson, 2016). A Bouguer gravity contour map of the Imperial Valley is overlain on the heat flow map (Biehler, 1964, 1971). The region exhibits a broad north-northwest positive Bouguer anomaly coincident with the axis of the trough. In this area, regions of gravity maxima often coincide with hydrothermal systems and high heat flow.

Our experiment, described in detail in Ajo-Franklin et al. (2022), was conducted in the Imperial Valley and utilized an unused fiber-optic telecommunication cable (dark fiber) starting in Calipatria, CA, running through Brawley and Imperial CA, and then turning West at El Centro, terminating in Plaster City. The total path length ($\sim$65 km) is too long for the DAS interrogator unit (IU, iDAS v2. Silixa LLC) used in this experiment to fully probe; only the first 28-km-partition, the black line in Figure 1, is utilized with a roughly straight path line crossing the previously hidden geothermal resources, BGF, and the complex transition zone, BSZ, where Brawley Fault lies.

The DAS IU is configured with 10 m gauge length and records strain-rate as the native unit; we used a 2 kHz laser pulse rate, which is higher than the sampling rate (500 Hz), to improve system dynamic range. The DAS channel locations are calibrated by tap tests along the fiber profile. After several acquisition tests, ambient noise data were continuously recorded at 4 m channel interval across the $\sim$28 km (total 6912 channels) dark fiber from Nov. 10th, 2020 till the spring of 2022. After first round of data retrieval in the spring of 2021, we obtained close to 4 months of continuous data (close to 65T) from Nov. 10th, 2020 to Mar. 8th, 2021. In this study, we utilize only the first two days to evaluate the feasibility of using DAS-based ambient noise data for high-resolution geothermal reservoir mapping. Details about experiment as well as installation information have been provided in Ajo-Franklin et al. (2022).

3 Methods

3.1 Noise Characteristics

Figure 2a shows a typical time domain ambient noise records from the 28-km-long DAS fiber with several identified seismic signatures associated with a variety of noise sources. Noise characteristics vary significantly across the profile. The signatures of moving vehicles are visible with linear moveouts, a common observation in urbanized areas on either dense nodal (Cheng et al., 2018, 2019) or DAS arrays (Ajo-Franklin et al., 2019; Wang et al., 2020; Rodríguez Tribaldos et al., 2021). A series of persistent noise sources are also observed across the DAS array, visible as stationary surface wave generators and highlighted by the dashed lines in Figure 2a. Examples include agricultural and transport infrastructure such as the grain silos and loading facility located around 0.9 km location, overpass excited in resonance around 15 km location, and an agriculture products wholesale facility around 16 km location. These powerful noise sources generate coherent surface waves propagating over multiple km, and contribute to extraction of coherent signals; however, the persistent localized sources with strong spatial consistency (almost zero moveout indicated by the vertical dashed lines) will produce nonnegligible spurious signals superimposed on empirical Green's functions (EGFs) during ambient noise interferometry, which will be discussed in later sections. Finally, towards the southern end of the array, increasing optical noise levels are observed due to the light propagation loss (Cedilnik et al., 2019; Waagaard et al., 2021) as well as the lack of traffic activities in the southern cropland area.

An averaged power spectrum (Figure 2b) of the first 2-day DAS ambient noise data along the cable shows that the dominant noise frequencies are located between 1 and 20 Hz, typical spectral characteristic for anthropogenic noise (Groos & Ritter, 2009; Cheng et al., 2019; Zhu & Stensrud, 2019). The variable spectrum at the southern end of the array indicates the lack of anthropogenic signals. It is worth mentioning that the slightly quieter interior section with dominant lower-frequency spectrum is located near the BGF.

3.2 Ambient Noise Interferometry

We utilized ambient noise interferometry to generate empirical Green's functions from the passive DAS data. Before interferometric processing, a sequence of steps were applied to reduce computational expense given the large array size and high temporal sampling. As an initial compression step, we temporally decimated the dataset to 100 Hz after applying an anti-aliasing filter; this step was followed by sequential spatial median stacking (5 trace window), which transformed the dataset from 6912 channels with a 4-meter spatial sampling interval to 1382 channels with 20-meter spatial sampling interval. This combination of spatial stacking and temporal decimation reduced the dataset size by about a factor of 25. Next, a classical ambient noise data preprocessing workflow (e.g., Bensen et al., 2007; Cheng et al., 2015, 2021a) was applied to the continuous DAS dataset (2 days) by processing 1 minute non-overlapping data segments with the native recording unit (strain rate). Preprocessing steps included mean and trend removal, as well as a symmetric Hanning taper applied to each end of the time series, followed by temporal and spectral normalization. The temporal normalization was accomplished using a running absolute mean filter. The spectral normalization step utilized a frequency-domain whitening approach, which exploits the smoothed amplitude of complex Fourier spectrum as the whitening weights (e.g., Bensen et al., 2007; Cheng et al., 2021b). To extract empirical Green's function (EGF) from the preprocessed ambient noise dataset, we utilized the cross-coherence algorithm by performing cross-correlation followed with spectral whitening (Schuster et al., 2004; Prieto et al., 2009; Nakata et al., 2011). According to Cheng et al. (2021a), the cross-coherence algorithm has advantages over the cross-correlation algorithm for mitigating pseudo-arrivals associated with spectral spikes and improving the signal to noise ratio (SNR) of the resulting EGF. After cross-coherence, we employ phase-weighted stacking (PWS) on 2 days of EGFs to further improve the coherent signals (Schimmel & Paulssen, 1997; Schimmel et al., 2011; Ventosa et al., 2017).

In the case of this dataset, special attention was paid to the effects of persistent localized noise sources, several of which are distributed across our array as discussed previously. Figure 3a displays an example of an extracted EGF gather with a virtual source at 1.2 km location (indicated by the red dashed line). Coherent signals are observed as far as $\sim$5 km offset range. Superimposed are three hyperbolic events centered at 0.9 km, 1.8 km and 2.6 km as highlighted with colored stars. The northernmost feature is identified as persistent noise from a grain silo complex; Figure 3b shows a photograph of the site's infrastructure where powerful and high-frequency ground vibrations were detected during tap test activities. The high frequency energy can also be observed on the averaged noise spectrum (Figure 2b). The other two dominant events are identified as source effects from crossing roads as indicated by the blue and magenta stars on the street map (Figure 3c). Compared with the energy from the grain silos, events from the persistent traffic noise usually show relatively lower frequencies and lower velocities. It is worth mentioning that the term "persistent localized source" in this work mainly indicates that the source is spatially persistent and temporally frequent, breaking the assumptions of randomly distributed noise sources underlying much of the theory of ambient noise imaging. Studies relevant to persistent localized noise sources have gained increasing attention with recent work ranging from source localization (Zeng & Ni, 2010) to seismic monitoring (Dales et al., 2017). However, these studies are usually limited by the sparse spatial sampling available with conventional seismic networks; DAS offers an alternative to study and utilize these persistent localized sources for potential seismic imaging and monitoring. Other recent studies have attempted to utilize these spurious events for structural seismic imaging (Yang et al., 2022), however, we believe they are not appropriate modes for such purposes. Our focus is on strategies to attenuate these persistent localized sources to improve conventional ambient noise imaging.

We developed a simple processing workflow to attenuate these spurious events associated with persistent localized noise sources and to enhance the SNRs of the resulting EGF. For conventional ambient noise imaging utilizing linear arrays and multichannel analysis of surface waves (MASW) technique, a roll-along strategy (Mayne, 1962; Xia et al., 2009) is often implemented by separating the array into a series of subarrays and rolling the subarrays to image subsurface lateral variations. In this approach, each subarray contains only one virtual-source cross-correlation/coherence gather with the first trace selected as the virtual-source (we refer to these as CN1 virtual-source gather, VSG) to ensure the uniform spatial coverage. In this study, CN1 virtual-source gathers are replaced by bin-offset stacked CN2 virtual-source gathers for each subarray where $C_N^2 = 1+2+...n-1$ and n is the trace number with each subarray. Here CN1 and CN2 are defined after the mathematic combination function. Bin-offset stacks simply stack all EGF source-receiver pairs that have the same spatial offset into a single super-gather. Bin-offset stacking techniques have been used for signal enhancement for 2-dimensional (2D) dense arrays (Nakata et al., 2015; Cheng et al., 2021a); we apply this technique to our dense 1-dimensional (1D) DAS array. In our approach, cross-coherence functions are first extracted for all possible inter-station pairs (CN2) after 2-day PWS stacking. The resulting gathers are then spatially averaged using bin-offset stacking to generate an enhanced VSG. This binning approach increases data quality, particularly for cross-coherence EGFs with small offsets, and tends to mitigate artifacts due to persistent noise sources and local lateral heterogeneity within each subarray. As a result, the stacked EGFs are more uniform, and generate more consistent dispersion curves that can be more effectively inverted using traditional surface wave analysis algorithms. However, as one would expect, some degree of lateral resolution is lost in the stacking process.

Figure 4 shows a typical example of the performance of CN2-bin-stack. Compared with the CN1 virtual-source gather (Figure 4a), the CN2-bin-stack virtual-source gather

(Figure 4b) has been significantly improved with attenuation of spurious arrivals associated with persistent localized sources and SNR enhancement as indicated by the trace-by-trace comparison shown in Figure 4c. The interval of the offset bins used in this work is 20 m, similar to the spatial sampling of the decimated dataset.

3.3 Surface wave imaging

As described above, a MASW roll-along strategy is implemented for ambient noise imaging. In order to ensure sufficient imaging depth and lateral resolution for geothermal reservoir characterization, a 5 km subarray was selected to allow observations of surface waves with sufficient wavelengths for constraining properties at a depth of ∼3 km (Xia et al., 2006; Foti et al., 2018). Subarrays roll along the DAS cable with a coverage overlap of 80% to ensure continuity of lateral variations beneath the DAS array. In total, we processed 57 subarrays across the DAS cable; for each subarray the enhanced VSG after CN2-bin-stack is analyzed for dispersion imaging and subsequent 1D shear wave velocity (V_s) inversion. Figure 5 depicts an integrated workflow of DAS ambient noise imaging developed for this study. In summary, the data processing workflow contains four steps, 1) data preprocessing which decimates the data matrices (from 415 Mb to ∼17Mb) and normalizes the time series (both temporal and spectral); 2) interferometric processing and stacking that generate one enhanced VSG for each subarray after CN2-bin-stack; 3) dispersion analysis based on the obtained VSG for each subarray; 4) V_s inversion, which constructs a series of 1D V_s profile for all subarrays and aligns them along the cable to build a pseudo-2D velocity structure.

We apply an improved frequency-domain slant-stacking algorithm (Cheng et al., 2021c) on each VSG for surface wave dispersion analysis. Figure 6 shows a typical example of the DAS-based surface wave retrieval (a) and dispersion image (b) at location ∼22 km. Clear Rayleigh waves with apparent velocities varying between 200 m/s to 800 m/s are visible on the enhanced VSG after CN2-bin-stack without interference from spurious arrivals associated with persistent localized sources. Higher overtones are clearly identified on the high-resolution dispersion spectrum. For accurate dispersion curve picking, we limit the target zone using the effective wavenumber range defined by $k_{min} = 1/L$ (L, array length 5 km) and $k_{max} = 1/dx$ (dx, spatial interval 20m) as indicated by the blue dashed lines on Figure 6b. Based on the enhanced surface wave shot gather and the high-resolution dispersion imaging technique, dispersion curves for multiple modes are picked across the DAS profile (see Figure S1 for all the picked curves in supporting information). Note that the offset information has been calibrated by tap tests results rather than the fixed channel interval, so that the geometry across the two curved sections around 6 km and 12 km locations will not impact phase velocity estimation.

To extract 1D V_s profile for each subarray, we simultaneously invert the multiple-mode Rayleigh wave dispersion curves by using a neighborhood algorithm (NA) as implemented in Geopsy (Wathelet et al., 2004). We initialize the V_s model based on the picked fundamental-mode dispersion curves by following the empirical formula described in Xia et al. (1999), and generate the density as well as the Poisson ratio model by interpolating from the IVLSU (Imperial Valley velocity model developed by Louisiana State University) model (Persaud et al., 2016; Ajala et al., 2019) archived in Unified Community Velocity Model (UCVM) package (Small et al., 2017) (see the initial models on Figure S2 in supporting information). To constrain the model space, we built an earth model pool with weak (±50% parametric perturbations) bounds based on the defined initial V_s model; density values are treated as a free parameter and P wave velocity (V_p) is linked to V_s during the inversion; layer number is fixed as defined in the initial model, and thickness of each layer is flexible with ±50% perturbations. For each subarray, we invert the multiple-mode dispersion curves with 3 independent runs of the inversion process. Each run retains 2500 models and the best 400 models of all runs are retained for velocity estimation. To reduce potential uncertainties within the neighborhood algorithm as well as avoid overfitting, we extract the optimal V_s model with a misfit-weighted mean model by averaging the best 100 models with weights from the corresponding misfits, rather than selecting the individual model with the smallest misfit. Figure 7 shows an example of a DAS-based surface wave inversion utilizing the multiple-mode dispersion curve picks from Figure 6b. For all modes, acceptable misfits between the measured and inverted dispersion curves are obtained (Figures 7a1-4). The forward modeled dispersion curves from the misfit-weighted model (the red curve in Figures 7b) also show a good match with the measured picks. Figure 8 shows the sensitivity kernels of different Rayleigh wave modes; compared with the sensitivity kernel of the fundamental mode (Figure 8a), higher sensitivities are observed at deeper depths for the lower frequency band of the first overtone (Figure 8b) and at shallower depth for higher frequencies of all the higher modes (Figure 8b-d). These observations indicate that simultaneous inversion of multiple modes has advantages over using only the fundamental mode, both reducing non-uniqueness and improving sensitivity at depth (Xia et al., 2012; L. Pan et al., 2019; Fu et al., 2022).

4 Results

Our high-resolution inverted V_s model, derived from the DAS array, is shown in Figure 9b with the prior IVLSU model shown for comparison (Figure 9a). While both models are broadly similar in depth, our inversion resolves a zone of high S-wave velocity beneath the BGF which is only hinted at in the IVLSU model. Likewise, the DAS result resolves two zones of lower S-wave velocity north and south of the BGF. The high velocity zone is also coincident with a region of shallow high V_p (see the reference V_p model on Figure S3 in the supporting information) observed in SSIP inversions (Han et al., 2016; Persaud et al., 2016). We hypothesize the feature is due to secondary mineral precipitation caused by hydrothermal brine circulation and corresponding water-rock interaction at depth.

At 5 km location where our DAS cable crosses over the Alamo River, a low-velocity zone (LVZ) is visible on the inverted V_s structure as indicated by the magenta arrow on Figure 9b, and coincides with the LVZ hinted at by the IVLSU model as indicated by the dip in the 1.5 km/s contour line around the 5 km location on Figure 9a. This LVZ might indicate an unmapped fault located between Calipatria and Brawley, considering similar discontinuities have been traced with correlations derived from electric logs (Towse, 1975), a ground magnetic survey (Meidav & Furgerson, 1972), and as well as a seismic refraction survey (Frith, 1978). Around the 20 km location, a prominent LVZ as indicated by the break contour line at 1.8 km/s on the DAS result is probably associated with the Brawley Fault (BF) and the complex fault network associated with the southern termination of the BSZ. The mapped BF from USGS Quaternary fault database crosses our cable at ∼21 km location on the surface (see Figure 1a), and our model indicates that it might extend farther to the north at depth.

In geothermal settings within sedimentary basins, high seismic velocities are often associated with low porosity units with high degrees of cementation and/or secondary alteration (e.g., Ryan & Shalev, 2014; McGuire et al., 2015). Additional knowledge of the ratio of P- to S-wave velocities (V_p/V_s) can help to further constrain subsurface properties and is sometimes more important than V_p or V_s separately in diagnosing the presence of fractures and the effects of pore pressure (Walck, 1988; Nakajima et al., 2001; Takei, 2002; Hamada, 2004; Behm et al., 2019). We utilize the V_p model from SSIP by slicing the three-dimensional (3D) model of Persaud et al. (2016) along our DAS cable and interpolating the 2D slice to the same grid as our inverted V_s model (see the reference V_p model on Figure S3 in the supporting information). Compared with the inverted 2D V_s model, however, the reference 2D V_p model lacks comparable spatial resolution due to the limited shots and receivers coverage in SSIP experiment. Although the obtained V_p/V_s model does not have as high a spatial resolution as the original V_s model, it is still a useful aid in interpreting the features beneath the BGF.

The resulting mapped V_p/V_s profile (Figure 10a) displays a prominent low V_p/V_s dome near the BGF area, as indicated by the contour line at $V_p/V_s = 1.8$. It coincides with the observation presented in Lin (2013) that one of the most significant features in the V_p/V_s model for Salton Trough is the predominantly low V_p/V_s values below 2 km depth and the lowest V_p/V_s ratios occur in the SSGF area, where the V_p/V_s ratios vary from 1.510 to 1.811 according to Lin (2020).

This low V_p/V_s feature is strikingly correlated with a high heat flow anomaly (the red curve in Figure 10b) as well as a gravity high (the blue curve in Figure 10b). The higher Bouguer gravity anomaly near the heat-flow anomaly (Figure 1b) may reflect a combination of two processes: (1) the intrusion of rhyolitic and basaltic dikes and sills, and/or (2) the increased density of sediments due to cementation, recrystallization, and thermal metamorphism generated by circulating hydrothermal fluids (Mase et al., 1981). Boreholes in geothermal areas in the Imperial Valley have encountered greenschist facies metamorphism, cementation of pore spaces, altered rhyolites, and basalt dikes. Many geologic studies of this area have concluded that hydrothermal alteration can have a pronounced effect on the physical properties of the sediments by reducing porosity and increasing density (Muffler & White, 1969; Robinson et al., 1976; Browne, 1976; McDowell & Elders, 1979; Elders et al., 1979; Miller & Elders, 1980). These hydrothermal alteration effects coincide with the observation of low V_p/V_s anomalies on Figure 10a, which might be used as an indicator for high temperature geothermal systems. In addition to the low V_p/V_s dome probably associated with the BGF geothermal reservoir, two high V_p/V_s zones around 5 km and 20 km locations are co-located with low velocity zones observed on the inverted V_s profile. We hypothesize that these features are damage zones related to faulting. Discontinuities in EGF waveform character, observed on common offset gathers derived from interferometric processing, also support above observations (see Figure S4 in the supporting information).

The Imperial Valley exhibits active deformation and seismicity associated with both extension within the rift centers and shear across strike-slip faults systems (Elders et al., 1972; Parsons & McCarthy, 1996; Han et al., 2016). Figure 1a shows the relocated historical earthquakes from 1981 to 2019 (Hauksson et al., 2012), with most of seismic events occurring in the BSZ, which represents the northernmost extension of the spreading center axis associated with the East Pacific Rise. In order to statistically analyze the distribution of seismicity along our DAS cable, we project the near-line (distance $<$ 2 km) events to the vertical plane where our DAS cable is located. Abundant earthquakes are distributed around the 20 km location (as shown on the histogram on Figure 10b); this observation is consistent with interpreting the high V_p/V_s values as damage related to faulting at the terminus of the BSZ. However, the relationship between the seismicity and the V_p/V_s distribution is still ambiguous considering the substantial offset between our inversion depth ($<$ 3 km) and the relocated earthquake depths mainly ranging from 5 km to 10 km (Hauksson et al., 2012). Earthquakes occurring in the BGF area at depths from 10 km to 15 km (much deeper than the geothermal reservoir) may have a remote connection to geothermal activities or at least related structures (Ellsworth, 2013); the histogram spike around 13.5 km is associated with the 2012 Brawley swarm (Wei et al., 2013), which has been hypothesized to be induced indirectly through poroelastic coupling rather than directly by a pore pressure change (Wei et al., 2015). During our DAS deployment, the primary seismic network observed no events close to the BGF, suggesting current production and injection activities are not inducing a large numbers of events.

5 Discussion

The Brawley geothermal field was originally developed by Union Oil Company (Unocal) in the 1970's. In addition to drilling deep geothermal wells, previous development included building and operating a 10 MWe power plant. Unfortunately, corrosion and scaling issues resulted in Unocal abandoning the project in the 1980's. Ormat Nevada

Inc investigated the potential of the shallow sands in 2006 and concluded that these matrix-permeable sands contained moderately saline water, high porosity, and could support a binary-type power plant. After resurrection of the previously developed geothermal field, a power plant with a nameplate capacity of 49.9 MWe is presently being operating (Matlick & Jayne, 2008).

To better evaluate the geothermal system beneath the Brawley field, we focus on the depth variation of the low V_p/V_s anomalies detected by DAS as well as observations from three nearby geothermal wells (see locations in Figure 1a). For better display, well logs are smoothed with a 150 m averaging window. Figure 11a provides a comparison between various velocity models in BGF area, which help us assess the reliability of the obtained structure models. Compared with the V_s model from the IVLSU (the blue dotted-dashed line), the inverted V_s model obtained using DAS (the gray solid line) shows higher vertical resolution; the reference V_p model (the blue dotted line) is smooth but generally matches the sonic log from the Veysey #1 geothermal well (the magenta line). We observe that the V_p/V_s model utilizing the reference V_p from Persaud et al. (2016) (the gray line in Figure 11b) matches well with the one with the reference V_p from the sonic log (the magenta line in Figure 11b), except for the shallower zones where the V_p model was poorly resolved from travel-time tomography in Persaud et al. (2016).

As shown in the high-resolution V_p/V_s profile (V_p from the sonic log), V_p/V_s gradually decreases until a depth of 800 m; then rapidly increases from 2.2 to 2.7 and then decreases to a relatively constant value ∼1.8 at depth below 1,600 m. We interpret the increasing V_p/V_s to be associated with the higher porosity upper geothermal reservoir dominated by matrix permeability. Historical logs show an increasing temperature from 100 to 170 ^{o}C with thermal gradients of approximately 85 ^{o}C/km (highlighted by the light-red shallow zone on Figure 11c). This interpretation is supported by the co-located geothermal production as indicated by the distribution of total depths of 18 new production wells (highlighted by the gray triangles on Figure 11b, c, and d).

We hypothesize the zone above to be an impermeable thermal cap with much higher V_p/V_s; however, the interface between the upper geothermal reservoir and the cap is ambiguous considering the lower resolution of the inverted V_s model comparing to the sonic log. The zone below with almost constant low V_p/V_s might house the lower geothermal reservoir with potential cementation, recrystallization and thermal metamorphism by circulating hydrothermal fluids. The increase in sulfide, chlorite, and epidote alteration noted in lithographic logs is indicative of hydrothermal activity (Elders & Sass, 1988; Paillet & Morin, 1988; Bonner et al., 2006).

This lower reservoir is also where Unocal detected the fractured high-temperature resource with fluid temperatures of up to 273 ^{o}C (the red square on Figure 11c) and operated the older production wells (the blue triangles on Figure 11b, c, and d). Unfortunately, high salinity brine and the non-condensable gas caused the carbon steel casing and surface equipment to rapidly develop scale and corrode; this problem led Unocal to abandon the project since the early exploration focus was on the higher temperature resources. While we would expect a higher V_p/V_s ratio in this zone due to fracturing, our surface wave study likely has insufficient resolving power to isolate such features at depth.

The constant temperature records in the lower reservoir with low gradients ∼1 ^{o}C/km might indicate the lower reservoir has been supplying heat to the cap long enough for steady-state conduction to develop. Due to thermal alteration, reduced porosity is observed in the lower reservoir compared to that in the upper reservoir (Figure 11d), consistent with both seismic observations and the Bouguer anomaly. The dominant heat transfer mechanism in the lower region might be convective flow of pore fluids. We refer to this region as the convective zone in contrast with the conductive zone. Figure 11e shows a simplified geothermal system including an impermeable thermal cap above 800 m, a relatively high porosity and conductive upper reservoir in the middle depth and a highly thermal-altered and convective lower reservoir below 1,600 m with localized regions of fracturing.

Our high-resolution 2D V_s profile from DAS ambient noise successfully mapped the high-temperature and highly thermally-altered lower geothermal reservoir. With the assistance of legacy sonic logs, the improved 1D V_p/V_s model with higher vertical resolution also detected the weakly thermal altered upper thermal reservoir, which contains moderately saline water and relatively high porosity. Unfortunately, it is challenging to distinguish this upper reservoir with ambient noise results alone due to the limited vertical resolution of the seismic imaging technique used. Further work is required to image fine-scale crustal structures beneath linear arrays, for example, waveform-based inversion method (Zhang et al., 2018; Y. Pan et al., 2021) or extraction of refracted body waves and/or reflected phases from the ambient noise wavefield.

6 Conclusions

We extract high quality surface waves from ambient noise data, acquired using DAS and a 28-km-long telecommunication cable, and apply high-resolution surface wave imaging to retrieve the S wave velocity structure of the top 3 km of the Imperial Valley. We develop a linear spatial stacking technique, called CN2-bin-stack, to attenuate spurious events associated with persistent localized sources and enhance the SNR of the retrieved EGF. We jointly invert multiple surface wave modes retrieved from this dataset to reduce non-uniqueness inherent in V_s inversion and improve sensitivity at depth. Based on the V_p model obtained from Persaud et al. (2016), we generate a 2D V_p/V_s profile across the valley, and observe a significant low V_p/V_s feature beneath the Brawley field, which is likely related to hydrothermal alteration within and beneath the currently producing reservoir. We have also identified two low velocity zones, north and south of the field, which we hypothesize are associated with an unmapped fault between Calipatria and Brawley and the mapped Brawley Fault and BSZ termination zone, respectively.

With the assistance of legacy sonic logs, we were also able to improve the 1D V_p/V_s model, allowing detection of the seismic signature associated with the upper geothermal reservoir. Based on observations from geothermal wells as well as heat flow and gravity surveys, a simplified geothermal system is inferred, incorporating an impermeable thermal cap above 800 m, a relatively high porosity and conductive upper reservoir at intermediate depths, and a highly altered, low porosity, and moderately fractured lower reservoir below 1,600 m. While future studies might benefit from incorporation of a larger variety of wave modes and earthquake signals recorded on the same network, our investigation effectively demonstrates the utility of high spatial-resolution geothermal characterization with DAS at the basin scale, as well as the potential for high temporal-resolution geothermal monitoring even with the short imaging period (2 days).

Data Availability Statement

The extracted empirical Green's functions, the picked dispersion curves and the inverted shear velocity model used in this work, as well as a small data chunk with 40-min raw DAS waveforms, are available in the following OSF repository: `https://osf.io/ckt9q`. Three geothermal wells used in Figure 11 are digitized from `https://www.conservation.ca.gov/` with API #02590043/02590182/02590183. The raw DAS dataset exceeds current repository limitations, but will be available in the near future through the Geothermal Data Repository (https://gdr.openei.org/); contact the corresponding author (`ja62@rice.edu`) for information.

Imperial Valley Dark Fiber Team

The Imperial Valley Dark Fiber (IVDF) Team includes Jonathan Ajo-Franklin (Rice University), Feng Cheng (Zhejiang University and Rice University), Verónica Rodríguez Tribaldos (LBNL), Avinash Nayak (LBNL), Todd Wood (LBNL), Michelle Robertson (LBNL), Kesheng Wu (LBNL), Bin Dong (LBNL), Patrick Dobson (LBNL), Robert Mellors (Scripps Institution of Oceanography), Cody Rotermund (ESnet and LBNL), Benxin Chi (Chinese Academy of Sciences, formerly Rice University); Eric Matzel (LLNL), Denise C. Templeton (LLNL), Christina Morency (LLNL).

Acknowledgments

The Imperial Valley Dark Fiber Project was supported by the Office of Energy Efficiency and Renewable Energy (EERE), Geothermal Technologies Office (GTO), U.S. Department of Energy (DOE) under Award Number DE-AC02-05CH11231 with Lawrence Berkeley National Laboratory (LBNL). We would like to thank Thomas Coleman and Silixa LLC for useful acquisition suggestions and Zayo for fiber access and field support at the Calipatria ILA. We are very grateful to Karina Mellors and Dave Sandwell for assistance with tap tests. We thanks Jacob DeAngelo of the USGS for providing heat flow data and Shengji Wei of the Nanyang Technological University for providing the location information of geothermal wells in BGF. We would also like to thank Prof. Shawn Biehler (UCR) for providing a subset of his gravity database relevant to our study and Naod Arya for assisting with obtaining and managing our wireline log collection. The 1981-2019 earthquake catalog for southern California is downloaded from Southern California Earthquake Data Center (SCEDC, last access Feb, 2022). The SCEDC and Southern California Seismic Network (SCSN) are funded through U.S. Geological Survey Grant G20AP00037, and the Southern California Earthquake Center, which is funded by NSF Cooperative Agreement EAR-0529922 and USGS Cooperative Agreement 07HQAG0008. The Quaternary faults is obtainde from USGS Quaternary fault database (https://usgs.maps.arcgis.com/apps/webappview We would like to acknowledge the use of the SCEC Unified Community Velocity Model Software (Small et al., 2017) in this research. Lastly, we thank John Akerley of Ormat for sharing data related to the Brawley geothermal field.

References

Ajala, R., Persaud, P., Stock, J. M., Fuis, G. S., Hole, J. A., Goldman, M., & Scheirer, D. (2019). Three-dimensional basin and fault structure from a detailed seismic velocity model of coachella valley, southern california. *Journal of Geophysical Research: Solid Earth*, *124*(5), 4728–4750.

Ajo-Franklin, J., Dou, S., Lindsey, N., Monga, I., Tracy, C., Robertson, M., … others (2019). Distributed acoustic sensing using dark fiber for near-surface characterization and broadband seismic event detection. *Scientific reports*, *9*(1), 1–14.

Ajo-Franklin, J., Rodríguez Tribaldos, V., Nayak, A., Cheng, F., Mellors, R., Chi, B., … Dobson, P. (2022). The Imperial Valley Dark Fiber Project: Towards seismic studies using DAS and telecom infrastructure for geothermal applications. *Seismological Research Letters*.

Anderson, E., Crosby, D., & Ussher, G. (2000). Bulls-eye! simple resistivity imaging to reliably locate the geothermal reservoir. In *Proceedings world geothermal congress* (pp. 909–914).

Ars, J.-M., Tarits, P., Hautot, S., Bellanger, M., Coutant, O., & Maia, M. (2019). Joint inversion of gravity and surface wave data constrained by magnetotelluric: application to deep geothermal exploration of crustal fault zone in felsic basement. *Geothermics*, *80*, 56–68.

Atef, H., Abd El-Gawad, A., Zaher, M. A., & Farag, K. (2016). The contribution of gravity method in geothermal exploration of southern part of the Gulf of

Suez-Sinai region, Egypt. *NRIAG Journal of Astronomy and Geophysics*, *5*(1), 173–185.

Behm, M., Cheng, F., Patterson, A., & Soreghan, G. (2019). Passive processing of active nodal seismic data: Estimation of Vp/Vs ratios to characterize structure and hydrology of an alpine valley infill. *Solid Earth*, 1–32. doi: 10.5194/se-2019-47

Bensen, G., Ritzwoller, M., Barmin, M., Levshin, A., Lin, F., Moschetti, M., ... Yang, Y. (2007). Processing seismic ambient noise data to obtain reliable broad-band surface wave dispersion measurements. *Geophysical Journal International*, *169*, 1239–1260.

Biehler, S. (1964). *A geophysical study of the Salton Trough of southern California* (Unpublished doctoral dissertation). California Institute of Technology.

Biehler, S. (1971). Gravity studies in the Imperial Valley. *Cooperative Geological-Geophysical-Geochemical Investigations of Geothermal Resources in the Imperial Valley of California: Riverside, California, University of California–Riverside Education Research Service*, 29–41.

Bonner, B., Hutchings, L., & Kasameyer, P. (2006). *A strategy for interpretation of microearthquake tomography results in the Salton Sea Geothermal Field based upon rock physics interpretations of state 2-14 borehole logs* (Tech. Rep.). Lawrence Livermore National Lab.(LLNL), Livermore, CA (United States).

Brodsky, E. E., & Lajoie, L. J. (2013). Anthropogenic seismicity rates and operational parameters at the salton sea geothermal field. *Science*, *341*(6145), 543–546.

Brogi, A., Lazzarotto, A., Liotta, D., Ranalli, G., Group, C. W., et al. (2005). Crustal structures in the geothermal areas of southern Tuscany (Italy): insights from the CROP 18 deep seismic reflection lines. *Journal of Volcanology and Geothermal Research*, *148*(1-2), 60–80.

Browne, P. (1976). *Occurrence of hydrothermal alteration of diabase Heber geothermal field, Imperial Valley, California. Preliminary results* (Tech. Rep.). University of California Riverside, Institute of Geophysics Planetary Physics Report.

Burton-Johnson, A., Dziadek, R., & Martin, C. (2020). Geothermal heat flow in antarctica: current and future directions. *The Cryosphere*, *14*(11), 3843–3873.

Campillo, M., & Paul, A. (2003). Long-range correlations in the diffuse seismic coda. *Science*, *299*(5606), 547–549.

Cedilnik, G., Lees, G., Schmidt, P., Herstrøm, S., & Geisler, T. (2019). Ultra-long reach fiber distributed acoustic sensing for power cable monitoring. In *Proceedings of the jicable* (Vol. 19).

Chalari, A., Mondanos, M., Coleman, T., Farhadiroushan, M., & Stork, A. (2019). Seismic methods for geothermal reservoir characterization and monitoring using fiber optic distributed acoustic and temperature sensor. In *Eage/bvg/fkpe joint workshop on borehole geophysics and geothermal energy* (Vol. 2019, pp. 1–6).

Chang, H., & Nakata, N. (2022). Investigation of time-lapse changes with das borehole data at the brady geothermal field using deconvolution interferometry. *Remote Sensing*, *14*(1), 185.

Cheng, F., Chi, B., Lindsey, N., Dawe, C., & Ajo-Franklin, J. (2021b). Utilizing distributed acoustic sensing and ocean bottom fiber optic cables for submarine structural characterization. *Scientific Reports*, *11*(1), 5613. doi: 10.1038/s41598-021-84845-y

Cheng, F., Lindsey, N. J., Sobolevskaia, V., Dou, S., Freifeld, B., Wood, T., ... Ajo-Franklin, J. B. (2022). Watching the cryosphere thaw: Seismic monitoring of permafrost degradation using distributed acoustic sensing during a controlled heating experiment. *Geophysical Research Letters*, *49*(10), e2021GL097195.

Cheng, F., Xia, J., Ajo-Franklin, J. B., Behm, M., Zhou, C., Dai, T., ... Zhou, C.

(2021a). High-resolution ambient noise imaging of geothermal reservoir using 3c dense seismic nodal array and ultra-short observation. *Journal of Geophysical Research: Solid Earth*, *126*(8), e2021JB021827.

Cheng, F., Xia, J., Behm, M., Hu, Y., & Pang, J. (2019). Automated Data Selection in the Tau–p Domain: Application to Passive Surface Wave Imaging. *Surveys in Geophysics*, 1–18. doi: 10.1007/s10712-019-09530-2

Cheng, F., Xia, J., Luo, Y., Xu, Z., Wang, L., Shen, C., ... Hu, Y. (2016). Multichannel analysis of passive surface waves based on cross-correlations. *Geophysics*, *81*(5), EN57–EN66.

Cheng, F., Xia, J., Xu, Y., Xu, Z., & Pan, Y. (2015). A new passive seismic method based on seismic interferometry and multichannel analysis of surface waves. *Journal of Applied Geophysics*, *117*, 126–135.

Cheng, F., Xia, J., Xu, Z., Hu, Y., & Mi, B. (2018). Frequency-wavenumber(FK)-based data selection in high-frequency passive surface wave survey. *Surveys in Geophysics*, *39*, 661–682.

Cheng, F., Xia, J., Zhang, K., Zhou, C., & Ajo-Franklin, J. B. (2021c). Phase-weighted slant-stacking for surface wave dispersion measurement. *Geophysical Journal International*, 256–269. doi: 10.1093/gji/ggab101

Combs, J. (1978). *Geothermal exploration techniques: a case study. Final report (Coso geothermal area).* (Tech. Rep.). Texas Univ., Richardson (USA). Center for Energy Studies.

Combs, J., & Hadley, D. (1977). Microearthquake investigation of the Mesa geothermal anomaly, Imperial Valley, California. *Geophysics*, *42*(1), 17–33.

Dales, P., Audet, P., & Olivier, G. (2017). Seismic interferometry using persistent noise sources for temporal subsurface monitoring. *Geophysical Research Letters*, *44*(21), 10–863.

Daley, T. M., Freifeld, B. M., Ajo-Franklin, J., Dou, S., Pevzner, R., Shulakova, V., ... others (2013). Field testing of fiber-optic distributed acoustic sensing (das) for subsurface seismic monitoring. *The Leading Edge*, *32*(6), 699–706.

Dobson, P. F. (2016). A review of exploration methods for discovering hidden geothermal systems. *GRC Transactions*, *40*, 695–706.

Dou, S., Lindsey, N., Wagner, A., Daley, T., Freifeld, B., Robertson, M., ... Ajo-Franklin, J. (2017). Distributed acoustic sensing for seismic monitoring of the near surface: A traffic-noise interferometry case study. *Scientific reports*, *7*(1), 1–12.

EIA. (2021). *Monthly energy review, April 2021* (Tech. Rep.). Energy Information Administration, Washington DC (United States). Retrieved from `https://www.eia.gov/totalenergy/data/monthly/pdf/mer.pdf`

Elders, W., Hoagland, J., McDowell, S., & Cobo, J. (1979). Hydrothermal mineral zones in the geothermal reservoir of Cerro Prieto. *Geothermics*, *8*(3-4), 201–209.

Elders, W., Rex, R., Robinson, P., Biehler, S., & Meidav, T. (1972). Crustal Spreading in Southern California: The Imperial Valley and the Gulf of California formed by the rifting apart of a continental plate. *Science*, *178*(4056), 15–24.

Elders, W., & Sass, J. (1988). The Salton Sea scientific drilling project. *Journal of Geophysical Research: Solid Earth*, *93*(B11), 12953–12968.

Ellsworth, W. L. (2013). Injection-induced earthquakes. *science*, *341*(6142), 1225942.

Fahnestock, M., Abdalati, W., Joughin, I., Brozena, J., & Gogineni, P. (2001). High geothermal heat flow, basal melt, and the origin of rapid ice flow in central Greenland. *Science*, *294*(5550), 2338–2342.

Feigl, K. L., & Parker, L. M. (2019). *Porotomo final technical report: Poroelastic tomography by adjoint inverse modeling of data from seismology, geodesy, and hydrology* (Tech. Rep.). Univ. of Wisconsin, Madison, WI (United States). doi: 10.2172/1499141

Feigl, K. L., & Team, P. (2017). Overview and preliminary results from the porotomo project at brady hot springs, nevada: Poroelastic tomography by adjoint inverse modeling of data from seismology, geodesy, and hydrology. In *42nd workshop on geothermal reservoir engineering* (pp. 1–15).

Fichtner, A., Bowden, D., & Ermert, L. (2020). Optimal processing for seismic noise correlations. *Geophysical Journal International*, *223*(3), 1548–1564.

Flóvenz, Ó. G., & Saemundsson, K. (1993). Heat flow and geothermal processes in iceland. *Tectonophysics*, *225*(1-2), 123–138.

Foti, S., Hollender, F., Garofalo, F., Albarello, D., Asten, M., Bard, P.-Y., ... others (2018). Guidelines for the good practice of surface wave analysis: a product of the InterPACIFIC project. *Bulletin of Earthquake Engineering*, *16*(6), 2367–2420.

Frith, R. B. (1978). *Seismic refraction investigation of the Salton Sea geothermal area, Imperial Valley, California* (Tech. Rep.). California Univ., Riverside (USA). Retrieved from https://www.osti.gov/servlets/purl/5716342

Fu, L., Pan, L., Li, Z., Dong, S., Ma, Q., & Chen, X. (2022). Improved high-resolution 3D Vs Model of Long Beach, CA: Inversion of multimodal dispersion curves from ambient noise of a dense array. *Geophysical Research Letters*. doi: 10.1029/2021GL097619

Fuis, G. S., Mooney, W. D., Healey, J. H., McMechan, G., & Lutter, W. (1982). Crustal structure of the Imperial Valley region. *US Geol. Surv. Prof. Pap*, *1254*, 25–49.

Gao, J., Zhang, H., Zhang, S., Chen, X., Cheng, Z., Jia, X., ... Xin, H. (2018). Three-dimensional magnetotelluric imaging of the geothermal system beneath the Gonghe Basin, Northeast Tibetan Plateau. *Geothermics*, *76*, 15–25.

Groos, J., & Ritter, J. (2009). Time domain classification and quantification of seismic noise in an urban environment. *Geophysical Journal International*, *179*(2), 1213–1231.

Guglielmetti, L., & Moscariello, A. (2021). On the use of gravity data in delineating geologic features of interest for geothermal exploration in the Geneva Basin (Switzerland): prospects and limitations. *Swiss Journal of Geosciences*, *114*(1), 1–20.

Hamada, G. (2004). Reservoir fluids identification using Vp/Vs ratio? *Oil & Gas Science and Technology*, *59*(6), 649–654.

Han, L., Hole, J. A., Stock, J. M., Fuis, G. S., Williams, C. F., Delph, J. R., ... Livers, A. J. (2016). Seismic imaging of the metamorphism of young sediment into new crystalline crust in the actively rifting Imperial Valley, California. *Geochemistry, Geophysics, Geosystems*, *17*(11), 4566–4584.

Hartog, A. H. (2017). *An introduction to distributed optical fibre sensors.* CRC press.

Hauksson, E., Stock, J., Bilham, R., Boese, M., Chen, X., Fielding, E. J., ... others (2013). Report on the august 2012 brawley earthquake swarm in imperial valley, southern california. *Seismological Research Letters*, *84*(2), 177–189.

Hauksson, E., Yang, W., & Shearer, P. M. (2012). Waveform relocated earthquake catalog for southern california (1981 to june 2011). *Bulletin of the Seismological Society of America*, *102*(5), 2239–2244.

Hill, D. P. (1977). A model for earthquake swarms. *Journal of Geophysical Research*, *82*(8), 1347–1352.

Hill, D. P., Mowinckel, P., & Peake, L. G. (1975). Earthquakes, active faults, and geothermal areas in the Imperial Valley, California. *Science*, *188*(4195), 1306–1308.

Jackson, D. D. (1981). *Seismic and geodetic studies of the Imperial Valley, California* (Tech. Rep.). Lawrence Livermore National Lab., CA (USA) and California Univ., Los Angeles.

Johnson, C. E., & Hadley, D. M. (1976). Tectonic implications of the Brawley earthquake swarm, Imperial valley, California, January 1975. *Bulletin of the Seismological Society of America*, *66*(4), 1133–1144.

Kasahara, J., Hasada, Y., Kuzume, H., Fujise, Y., Mikada, H., & Yamamoto, K. (2020). Seismic feasibility study to identify and characterize supercritical geothermal reservoirs using dts, das, and surface seismic array. In *Proceedings world geothermal congress* (p. 1).

Kaspereit, D., Mann, M., Sanyal, S., Rickard, B., Osborn, W., & Hulen, J. (2016). Updated conceptual model and reserve estimate for the Salton Sea geothermal field, Imperial Valley, California. *Geotherm. Res. Council Trans*, *40*, 57–66.

Lachenbruch, A., & Sass, J. (1973). Thermo-mechanical aspects of the San Andreas fault system. In *Proceedings of the conference on the tectonic problems of the san andreas fault system* (Vol. 13, pp. 192–205).

Larson, R. L., Menard, H., & Smith, S. (1968). Gulf of California: a result of ocean-floor spreading and transform faulting. *Science*, *161*(3843), 781–784.

Lehujeur, M., Vergne, J., Schmittbuhl, J., Zigone, D., Le Chenadec, A., & Team, E. (2018). Reservoir imaging using ambient noise correlation from a dense seismic network. *Journal of Geophysical Research: Solid Earth*, *123*(8), 6671–6686.

Lellouch, A., Lindsey, N. J., Ellsworth, W. L., & Biondi, B. L. (2020). Comparison between distributed acoustic sensing and geophones: Downhole microseismic monitoring of the forge geothermal experiment. *Seismological Society of America*, *91*(6), 3256–3268.

Lellouch, A., Schultz, R., Lindsey, N. J., Biondi, B., & Ellsworth, W. L. (2021). Low-magnitude seismicity with a downhole distributed acoustic sensing array—examples from the forge geothermal experiment. *Journal of Geophysical Research: Solid Earth*, *126*(1), e2020JB020462.

Lin, G. (2013). Three-dimensional seismic velocity structure and precise earthquake relocations in the Salton trough, southern California. *Bulletin of the Seismological Society of America*, *103*(5), 2694–2708.

Lin, G. (2020). Spatiotemporal variations of in situ Vp/Vs ratio within the Salton Sea Geothermal Field, southern California. *Geothermics*, *84*, 101740.

Lin, G., Shearer, P. M., & Hauksson, E. (2007). Applying a three-dimensional velocity model, waveform cross correlation, and cluster analysis to locate southern california seismicity from 1981 to 2005. *Journal of Geophysical Research: Solid Earth*, *112*(B12).

Lindsey, N. J., & Martin, E. R. (2021). Fiber-optic seismology. *Annual Review of Earth and Planetary Sciences*, *49*, 309–336.

Lindsey, N. J., Martin, E. R., Dreger, D. S., Freifeld, B., Cole, S., James, S. R., ... Ajo-Franklin, J. B. (2017). Fiber-optic network observations of earthquake wavefields. *Geophysical Research Letters*, *44*(23), 11–792.

Lindsey, N. J., Rademacher, H., & Ajo-Franklin, J. B. (2020). On the broadband instrument response of fiber-optic DAS arrays. *Journal of Geophysical Research: Solid Earth*, *125*(2), e2019JB018145.

Lohman, R., & McGuire, J. (2007). Earthquake swarms driven by aseismic creep in the salton trough, california. *Journal of Geophysical Research: Solid Earth*, *112*(B4).

Lomnitz, C., Mooser, F., Allen, C. R., Brune, J. N., & Thatcher, W. (1970). Seismicity and tectonics of the northern Gulf of California region, Mexico. Preliminary results. *Geofisica Internacional*, *10*(2), 37–48.

Lüschen, E., Dussel, M., Thomas, R., & Schulz, R. (2011). 3D seismic survey for geothermal exploration at Unterhaching, Munich, Germany. *First Break*, *29*(1).

Marone, C. J., Scholtz, C., & Bilham, R. (1991). On the mechanics of earthquake afterslip. *Journal of Geophysical Research: Solid Earth*, *96*(B5), 8441–8452.

Martin, E. R., Lindsey, N. J., Ajo-Franklin, J. B., & Biondi, B. L. (2021). Introduction to interferometry of fiber-optic strain measurements. *Distributed Acoustic*

Sensing in Geophysics: Methods and Applications, 111–129.

Martins, J. E., Ruigrok, E., Draganov, D., Hooper, A., Hanssen, R., White, R., & Soosalu, H. (2019). Imaging Torfajökull's magmatic plumbing system with seismic interferometry and phase velocity surface wave tomography. *Journal of Geophysical Research: Solid Earth*, *124*(3), 2920–2940.

Martins, J. E., Weemstra, C., Ruigrok, E., Verdel, A., Jousset, P., & Hersir, G. (2020). 3D S-wave velocity imaging of Reykjanes Peninsula high-enthalpy geothermal fields with ambient-noise tomography. *Journal of Volcanology and Geothermal Research*, *391*, 106685.

Mase, C., Sass, J., Brook, C., & Munroe, R. J. (1981). *Shallow hydrothermal regime of the East Brawley and Glamis known geothermal resource areas, Salton Trough, California* (Tech. Rep.). Geological Survey, Washington, DC (USA).

Masoudi, A., & Newson, T. P. (2016). Contributed review: Distributed optical fibre dynamic strain sensing. *Review of scientific instruments*, *87*(1), 011501.

Matlick, S., & Jayne, T. (2008). Brawley—resurrection of a previously developed geothermal field. *GRC Transactions*, *32*, 159–162.

Mayne, W. H. (1962). Common reflection point horizontal data stacking techniques. *Geophysics*, *27*(6), 927–938.

McDowell, S., & Elders, W. (1979). Geothermal metamorphism of sandstone in the salton sea geothermal system. *Guidebook: Geology and Geothermics of the. Salton Trough*, 70–76.

McGuire, J. J., Lohman, R. B., Catchings, R. D., Rymer, M. J., & Goldman, M. R. (2015). Relationships among seismic velocity, metamorphism, and seismic and aseismic fault slip in the Salton Sea Geothermal Field region. *Journal of Geophysical Research: Solid Earth*, *120*(4), 2600–2615.

Meidav, T., & Furgerson, R. (1972). Resistivity studies of the Imperial Valley geothermal area, California. *Geothermics*, *1*(2), 47–62.

Miller, K. R., & Elders, W. A. (1980). *Geology, hydrothermal petrology, stable isotope geochemistry, and fluid inclusion geothermometry of LASL geothermal test well C/T-1 (Mesa 31-1), East Mesa, Imperial Valley, California, USA* (Tech. Rep.). California Univ., Riverside (USA). Inst. of Geophysics and Planetary Physics.

Muffler, L. P., & White, D. E. (1969). Active metamorphism of upper Cenozoic sediments in the Salton Sea geothermal field and the Salton Trough, southeastern California. *Geological Society of America Bulletin*, *80*(2), 157–181.

Munoz, G. (2014). Exploring for geothermal resources with electromagnetic methods. *Surveys in geophysics*, *35*(1), 101–122.

Nakajima, J., Matsuzawa, T., Hasegawa, A., & Zhao, D. (2001). Three-dimensional structure of Vp, Vs, and Vp/Vs beneath northeastern Japan: Implications for arc magmatism and fluids. *Journal of Geophysical Research: Solid Earth*, *106*(B10), 21843–21857.

Nakata, N., Chang, J. P., Lawrence, J. F., & Boué, P. (2015). Body wave extraction and tomography at Long Beach, California, with ambient-noise interferometry. *Journal of Geophysical Research: Solid Earth*, *120*(2), 1159–1173. doi: 10.1002/2015JB011870

Nakata, N., Snieder, R., Tsuji, T., Larner, K., & Matsuoka, T. (2011). Shear wave imaging from traffic noise using seismic interferometry by cross-coherence. *Geophysics*, *76*(6), SA97–SA106.

Paillet, F. L., & Morin, R. H. (1988). Analysis of geophysical well logs obtained in the State 2–14 borehole, Salton Sea geothermal area, California. *Journal of Geophysical Research: Solid Earth*, *93*(B11), 12981–12994.

Paitz, P., Edme, P., Gräff, D., Walter, F., Doetsch, J., Chalari, A., . . . Fichtner, A. (2021). Empirical investigations of the instrument response for distributed acoustic sensing (DAS) across 17 octaves. *Bulletin of the Seismological Society of America*, *111*(1), 1–10.

Pan, L., Chen, X., Wang, J., Yang, Z., & Zhang, D. (2019). Sensitivity analysis of dispersion curves of rayleigh waves with fundamental and higher modes. *Geophysical Journal International*, *216*(2), 1276–1303.

Pan, Y., Gao, L., & Bohlen, T. (2021). Random-objective waveform inversion of 3d-9c shallow-seismic field data. *Journal of Geophysical Research: Solid Earth*, *126*(9), e2021JB022036.

Parsons, T., & McCarthy, J. (1996). Crustal and upper mantle velocity structure of the Salton Trough, southeast California. *Tectonics*, *15*(2), 456–471.

Persaud, P., Ma, Y., Stock, J. M., Hole, J. A., Fuis, G. S., & Han, L. (2016). Fault zone characteristics and basin complexity in the southern Salton Trough, California. *Geology*, *44*(9), 747–750.

Planès, T., Obermann, A., Antunes, V., & Lupi, M. (2020). Ambient-noise tomography of the Greater Geneva Basin in a geothermal exploration context. *Geophysical Journal International*, *220*(1), 370–383.

Prieto, G., Lawrence, J., & Beroza, G. (2009). Anelastic earth structure from the coherency of the ambient seismic field. *Journal of Geophysical Research: Solid Earth*, *114*(B7).

Robins, J. C., Kolker, A., Flores-Espino, F., Pettitt, W., Schmidt, B., Beckers, K., ... Anderson, B. (2021). *2021 US Geothermal Power Production and District Heating Market Report* (Tech. Rep.). National Renewable Energy Lab.(NREL), Golden, CO (United States). Retrieved from `https://www.nrel.gov/docs/fy21osti/78291.pdf`

Robinson, P. T., Elders, W. A., & Muffler, L. P. (1976). Quaternary volcanism in the Salton Sea geothermal field, Imperial Valley, California. *Geological Society of America Bulletin*, *87*(3), 347–360.

Rodríguez Tribaldos, V., Ajo-Franklin, J., Dou, S., Lindsey, N. J., Ulrich, C., Robertson, M., ... Tracy, C. (2021). Surface wave imaging using distributed acoustic sensing deployed on dark fiber: Moving beyond high-frequency noise. *Distributed Acoustic Sensing in Geophysics: Methods and Applications*, 197–212.

Ryan, G. A., & Shalev, E. (2014). Seismic velocity/temperature correlations and a possible new geothermometer: Insights from exploration of a high-temperature geothermal system on montserrat, west indies. *Energies*, *7*(10), 6689–6720.

Santos, P. A., & Rivas, J. A. (2009). Gravity survey contribution to geothermal exploration in El Salvador: The cases of Berlín, Ahuachapán and San Vicente Areas. *LaGeo SA de CV United Nations University Geothermal Training Program*.

Sbrana, A., Lenzi, A., Paci, M., Gambini, R., Sbrana, M., Ciani, V., & Marianelli, P. (2021). Analysis of natural and power plant CO2 emissions in the Mount Amiata (Italy) volcanic–geothermal area reveals sustainable electricity production at zero emissions. *Energies*, *14*(15), 4692.

Schimmel, M., & Paulssen, H. (1997). Noise reduction and detection of weak, coherent signals through phase weighted stacks. *Geophysical Journal International*, *130*, 497–505.

Schimmel, M., Stutzmann, E., & Gallart, J. (2011). Using instantaneous phase coherence for signal extraction from ambient noise data at a local to a global scale. *Geophysical Journal International*, *184*(1), 494–506.

Schölderle, F., Lipus, M., Pfrang, D., Reinsch, T., Haberer, S., Einsiedl, F., & Zosseder, K. (2021). Monitoring cold water injections for reservoir characterization using a permanent fiber optic installation in a geothermal production well in the southern german molasse basin. *Geothermal Energy*, *9*(1), 1–36.

Schuster, G., Yu, J., Sheng, J., & Rickett, J. (2004). Interferometric/daylight seismic imaging. *Geophysical Journal International*, *157*(2), 838–852.

Shapiro, N. M., & Campillo, M. (2004). Emergence of broadband rayleigh waves from correlations of the ambient seismic noise. *Geophysical Research Letters*,

31(7).
Small, P., Gill, D., Maechling, P. J., Taborda, R., Callaghan, S., Jordan, T. H., ... Goulet, C. (2017). The SCEC unified community velocity model software framework. *Seismological Research Letters*, *88*(6), 1539–1552.
Snieder, R. (2004). Extracting the Green's function from the correlation of coda waves: A derivation based on stationary phase. *Physical Review E*, *69*(4), 046610.
Snieder, R., Miyazawa, M., Slob, E., Vasconcelos, I., & Wapenaar, K. (2009). A comparison of strategies for seismic interferometry. *Surveys in Geophysics*, *30*(4-5), 503–523.
Soyer, W., Mackie, R., Hallinan, S., Pavesi, A., Nordquist, G., Suminar, A., ... Nelson, C. (2018). Geologically consistent multiphysics imaging of the Darajat geothermal steam field. *First Break*, *36*(6), 77–83.
Spica, Z. J., Nakata, N., Liu, X., Campman, X., Tang, Z., & Beroza, G. C. (2018, jul). The ambient seismic field at Groningen Gas Field: An overview from the surface to reservoir depth. *Seismological Research Letters*, *89*(4), 1450–1466. doi: 10.1785/0220170256
Takei, Y. (2002). Effect of pore geometry on Vp/Vs: From equilibrium geometry to crack. *Journal of Geophysical Research: Solid Earth*, *107*(B2), ECV–6.
Thanassoulas, C. (1991). Geothermal exploration using electrical methods. *Geoexploration*, *27*(3-4), 321–350.
Towse, D. (1975). *An estimate of the geothermal energy resource in the Salton Trough, California. UCRL-51851 (Rev.1).* (Tech. Rep.). California Univ., Livermore (USA). Lawrence Livermore Lab. Retrieved from https://www.osti.gov/biblio/7353985
Tyler, S. W., Selker, J. S., Hausner, M. B., Hatch, C. E., Torgersen, T., Thodal, C. E., & Schladow, S. G. (2009). Environmental temperature sensing using raman spectra dts fiber-optic methods. *Water Resources Research*, *45*(4).
Ventosa, S., Schimmel, M., & Stutzmann, E. (2017). Extracting surface waves, hum and normal modes: time-scale phase-weighted stack and beyond. *Geophysical Journal International*, *211*(1), 30–44.
Waagaard, O. H., Rønnekleiv, E., Haukanes, A., Stabo-Eeg, F., Thingbø, D., Forbord, S., ... Brenne, J. K. (2021). Real-time low noise distributed acoustic sensing in 171 km low loss fiber. *OSA Continuum*, *4*(2), 688–701.
Walck, M. C. (1988). Three-dimensional Vp/Vs variations for the Coso region, California. *Journal of Geophysical Research: Solid Earth*, *93*(B3), 2047–2052.
Wang, X., Williams, E. F., Karrenbach, M., Herráez, M. G., Martins, H. F., & Zhan, Z. (2020). Rose parade seismology: Signatures of floats and bands on optical fiber. *Seismological Research Letters*, *91*(4), 2395–2398.
Wapenaar, K. (2004). Retrieving the elastodynamic Green's function of an arbitrary inhomogeneous medium by cross correlation. *Physical Review Letters*, *93*(25), 254301.
Ward, P. L. (1972). Microearthquakes: prospecting tool and possible hazard in the development of geothermal resources. *Geothermics*, *1*(1), 3–12.
Wathelet, M., Jongmans, D., & Ohrnberger, M. (2004). Surface-wave inversion using a direct search algorithm and its application to ambient vibration measurements. *Near Surface Geophysics*, *2*(4), 211–221.
Wei, S., Avouac, J.-P., Hudnut, K. W., Donnellan, A., Parker, J. W., Graves, R. W., ... others (2015). The 2012 brawley swarm triggered by injection-induced aseismic slip. *Earth and Planetary Science Letters*, *422*, 115–125.
Wei, S., Helmberger, D., Owen, S., Graves, R. W., Hudnut, K. W., & Fielding, E. J. (2013). Complementary slip distributions of the largest earthquakes in the 2012 brawley swarm, imperial valley, california. *Geophysical Research Letters*, *40*(5), 847–852.
Williams, C., Reed, M., Galanis Jr, S., & DeAngelo, J. (2007). The USGS na-

tional geothermal resource assessment: An update. In *Geothermal resources council-annual meeting of the geothermal resources council 2007* (Vol. 31, pp. 99–104).

Williams, C., Reed, M. J., DeAngelo, J., & Galanis Jr, S. P. (2009). Quantifying the undiscovered geothermal resources of the united states. In *Geothermal resources council 2009 annual meeting* (Vol. 33).

Williams, C., Reed, M. J., Mariner, R. H., DeAngelo, J., & Galanis, S. P. (2008). *Assessment of moderate-and high-temperature geothermal resources of the United States* (Tech. Rep.). Geological Survey (US). Retrieved from http://pubs.usgs.gov/fs/2008/3082

Winker, C. D. (1987). *Neogene stratigraphy of the Fish Creek-Vallecito section, southern California: Implications for early history of the northern Gulf of California and Colorado delta (San Andreas Fault).* The University of Arizona.

Xia, J., Miller, R. D., & Park, C. B. (1999). Estimation of near-surface shear-wave velocity by inversion of rayleigh waves. *Geophysics*, *64*(3), 691–700.

Xia, J., Miller, R. D., Xu, Y., Luo, Y., Chen, C., Liu, J., … Zeng, C. (2009). High-frequency rayleigh-wave method. *Journal of Earth Science*, *20*(3), 563–579.

Xia, J., Xu, Y., Chen, C., Kaufmann, R. D., & Luo, Y. (2006). Simple equations guide high-frequency surface-wave investigation techniques. *Soil Dynamics and Earthquake Engineering*, *26*(5), 395–403.

Xia, J., Xu, Y., Luo, Y., Miller, R. D., Cakir, R., & Zeng, C. (2012). Advantages of using multichannel analysis of Love waves (MALW) to estimate near-surface shear-wave velocity. *Surveys in Geophysics*, *33*(5), 841–860.

Yang, Y., Zhan, Z., Shen, Z., & Atterholt, J. (2022). Fault zone imaging with distributed acoustic sensing: Surface-to-surface wave scattering. *Journal of Geophysical Research: Solid Earth*, e2022JB024329.

Zeng, X., & Ni, S. (2010). A persistent localized microseismic source near the Kyushu Island, Japan. *Geophysical Research Letters*, *37*(24), 8–13. doi: 10.1029/2010GL045774

Zhan, Z. (2020). Distributed acoustic sensing turns fiber-optic cables into sensitive seismic antennas. *Seismological Research Letters*, *91*(1), 1–15.

Zhang, C., Yao, H., Liu, Q., Zhang, P., Yuan, Y. O., Feng, J., & Fang, L. (2018). Linear array ambient noise adjoint tomography reveals intense crust-mantle interactions in North China Craton. *Journal of Geophysical Research: Solid Earth*, *123*(1), 368–383.

Zhou, C., Xia, J., Pang, J., Cheng, F., Chen, X., Xi, C., … Zhou, C. (2021, may). Near-Surface geothermal reservoir imaging based on the customized dense seismic network. *Surveys in Geophysics*, *42*(3), 673–697. doi: 10.1007/s10712-021-09642-8

Zhu, T., & Stensrud, D. J. (2019). Characterizing thunder–induced ground motions using fiber-optic distributed acoustic sensing array. *Journal of Geophysical Research: Atmospheres*, 810–823. doi: 10.1029/2019JD031453

Zucca, J., Hutchings, L., & Kasameyer, P. (1994). Seismic velocity and attenuation structure of the geysers geothermal field, california. *Geothermics*, *23*(2), 111–126.

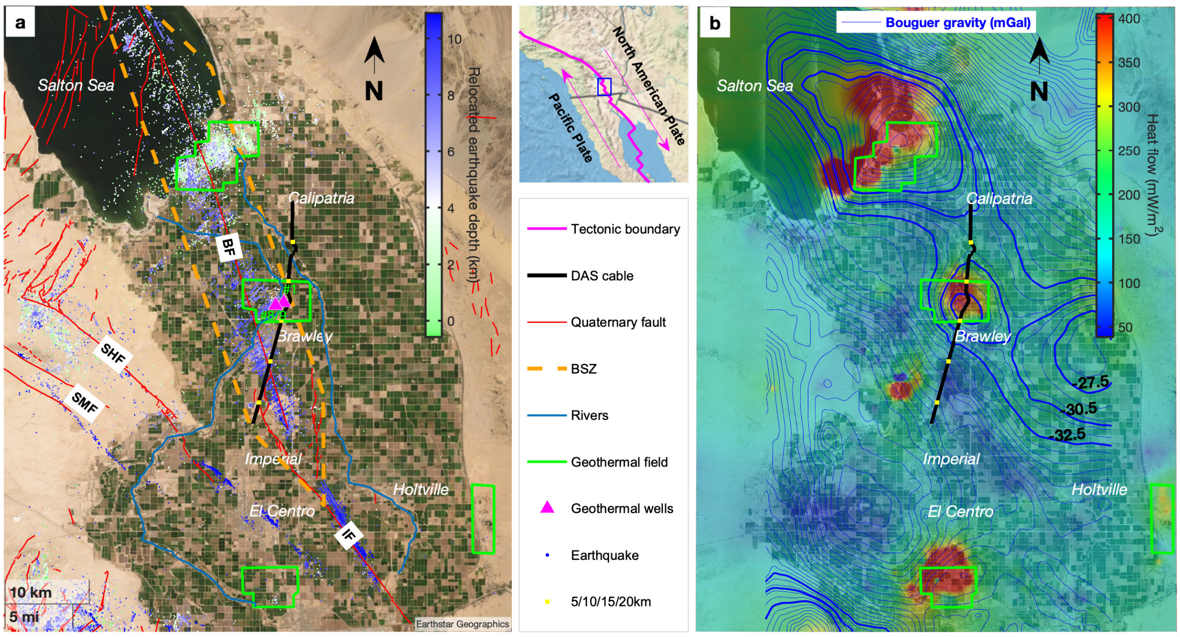

Figure 1. Site overview of the Imperial Valley dark fiber experiment. (a). Maps of the Imperial Valley with DAS cable array (black line), Quaternary faults (red lines), Brawley seismic zone (orange dash-line polygon), rivers (Alamo River and New River, steelblue lines), geothermal fields (green polygons), geothermal wells (magenta triangles, #1, #8 and #9) discussed in this paper, and historical earthquakes from 1981 to 2019 (blue-to-green colored dots). The colors of earthquakes are coded by the relocated depths (Hauksson et al., 2012). 5 yellow squares mark the cable length at 5/10/15/20/25 km locations referring to the north starting end. Major faults in the region are indicated by capital letters as follows: Imperial Fault (IF), Superstition Hills Fault (SHF), Superstition Mountain Fault (SMF) and Brawley Fault (BF). (b). Heat flow map (Williams et al., 2007, 2008) of the Imperial valley area overlaying with Bouguer gravity contours (blue lines) (Biehler, 1964, 1971).

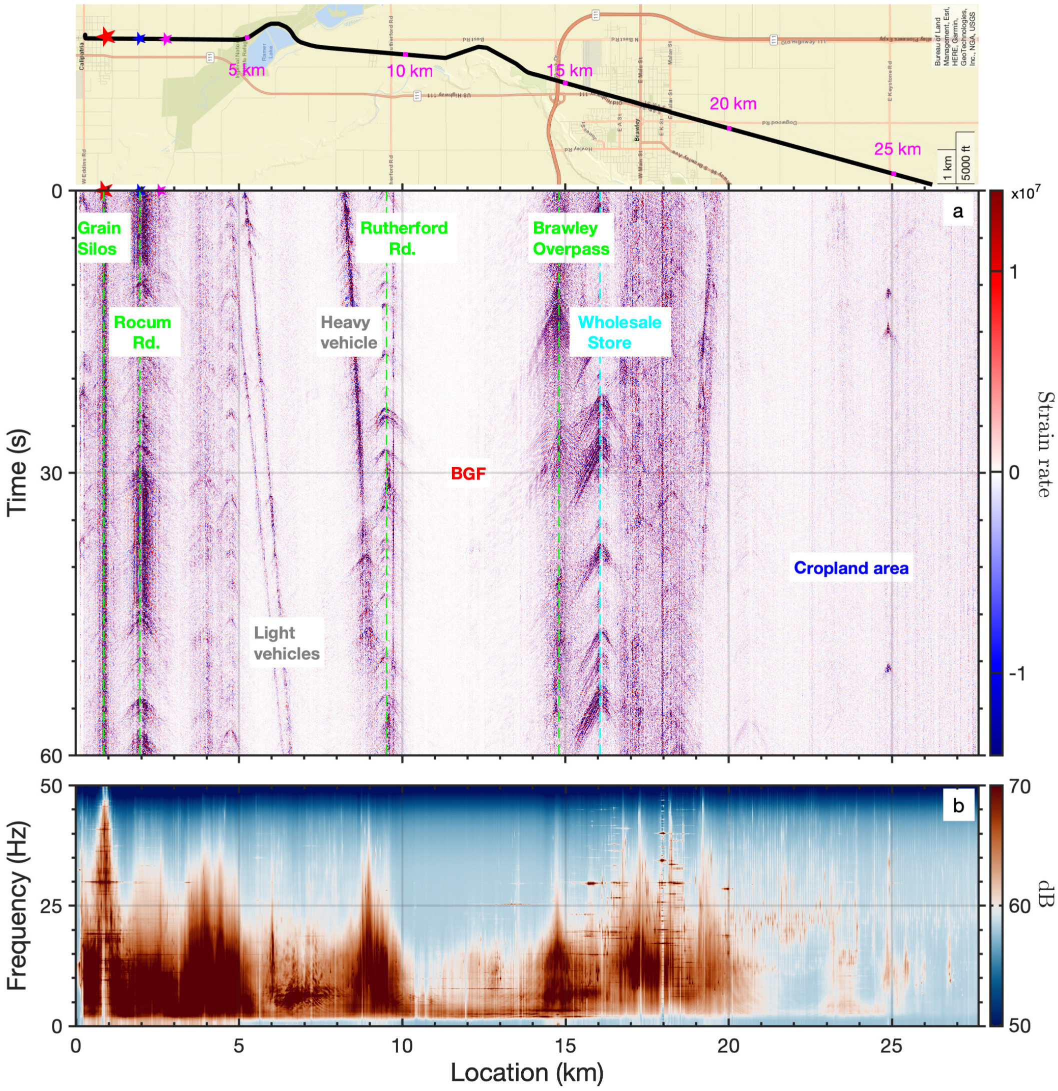

Figure 2. Observations of ambient noise on a ∼28 km DAS array. (a) 60-second-long ambient noise record in strain-rate (unit, nanostrain/s) with seismic signatures from moving vehicles and persistent localized sources, like factories, crossing roads, Brawley overpass, and Brawley Airport. A rotated street map on the top of (a) shows the main infrastructures crossing the cable. Three colored stars, colocated on both street map and the waveform map, represent the detected persistent localized sources, like grain silos (the red star) and crossing roads (the blue stars). (b) 2-day averaged spectrum of the noise along the cable.

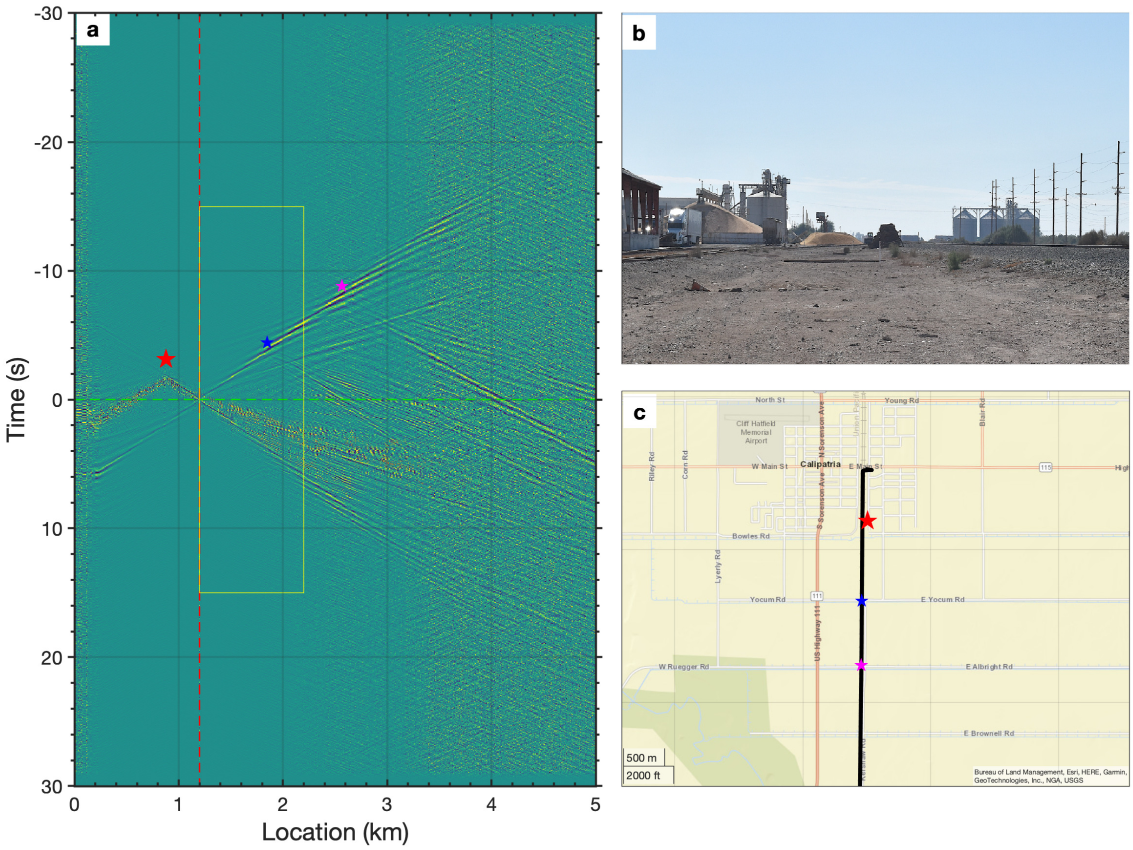

Figure 3. Example of the effect from persistent localized source. (a) Empirical Green's function gather with virtual source at 1.2 km location (indicated by the red dashed line). The colored stars indicate the persistent localized sources, from the working grain silo (red star), the Yocum Rd (blue star) and the Albright Rd (magenta star), which have been colocted on the raw waveform map. (b) shows the site photo of the grain silo beside the cable line as indicated by the red star on (c). The street map on (c) shows the Yocum Rd and the Albright Rd crossing the fiber-optic cable (the black line). Seismic signature of the grain silo is significantly different to that of the crossing roads and shows dominant higher frequency components.

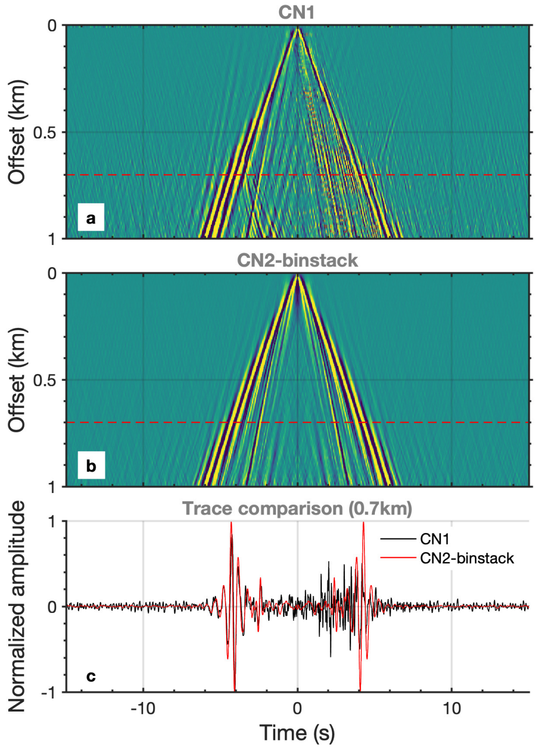

Figure 4. Performance of CN2-bin-stack. (a) The CN1 shot gather with the first channel as virtual source and the other N channels as virtual receivers. (b) The CN2-bin-stack shot gather with every channel as virtual source and the channels behind the virtual sources as virtual receivers. (c) Single trace comparison between CN1 (black) and CN2-bin-stack (red) shot gather at offset 0.7 km (highlighted by the red dashed line in (a) and (b)).

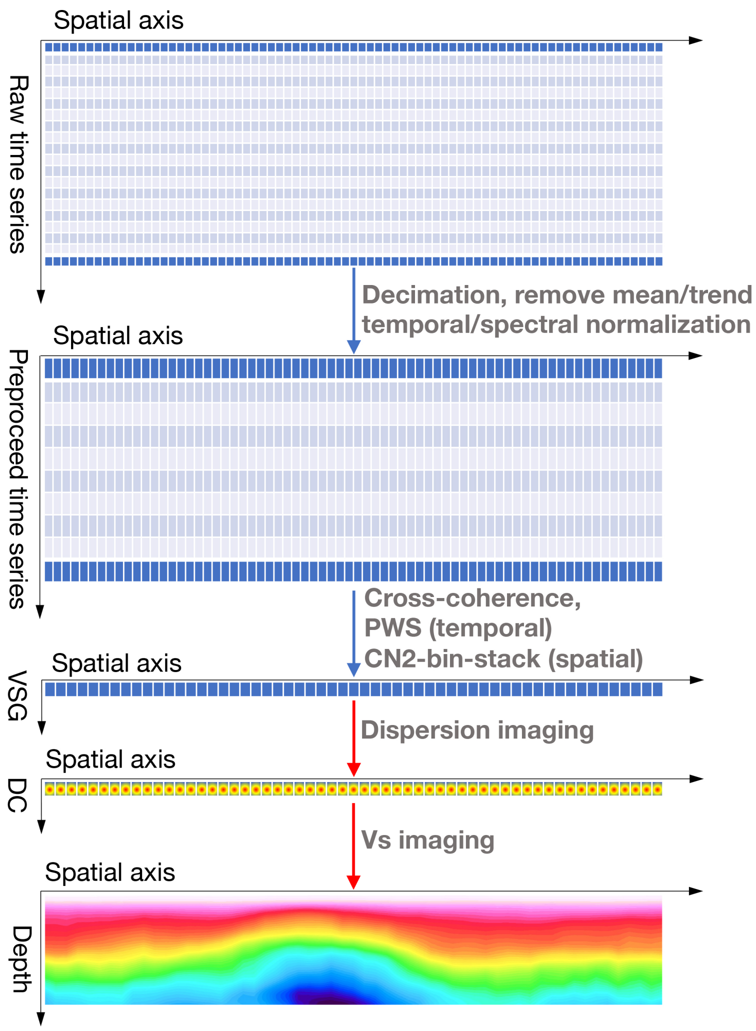

Figure 5. Workflow of DAS ambient noise imaging including preprocessing, virtual source gather (VSG) generation, dispersion curve (DC) measurement, and S-wave inversion.

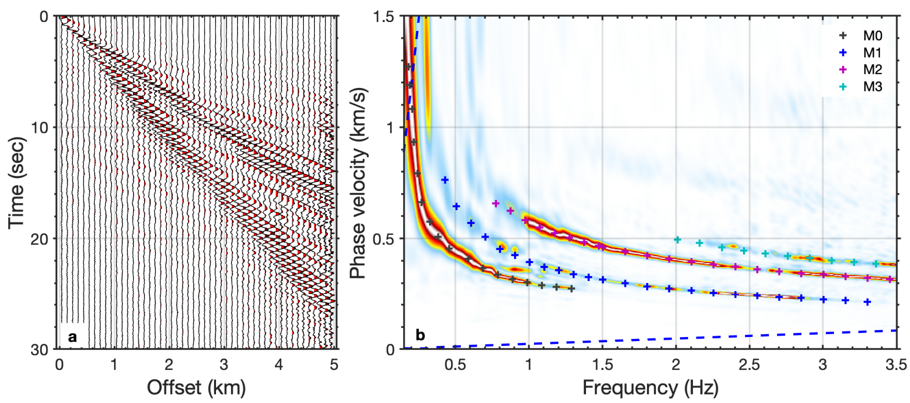

Figure 6. DAS-based surface wave retrieval and dispersion analysis. (a) and (b) show the extracted Rayleigh wave shot gather after CN2-bin-stack and the corresponding dispersion measurement with multiple modes identified and picked. The blue dashed lines indicate the minimum wavenumber defined by k_{min}=1/L (L, array length) and the maximum wavenumber defined by $k_{max} = 1/dx$ (dx, spatial interval).

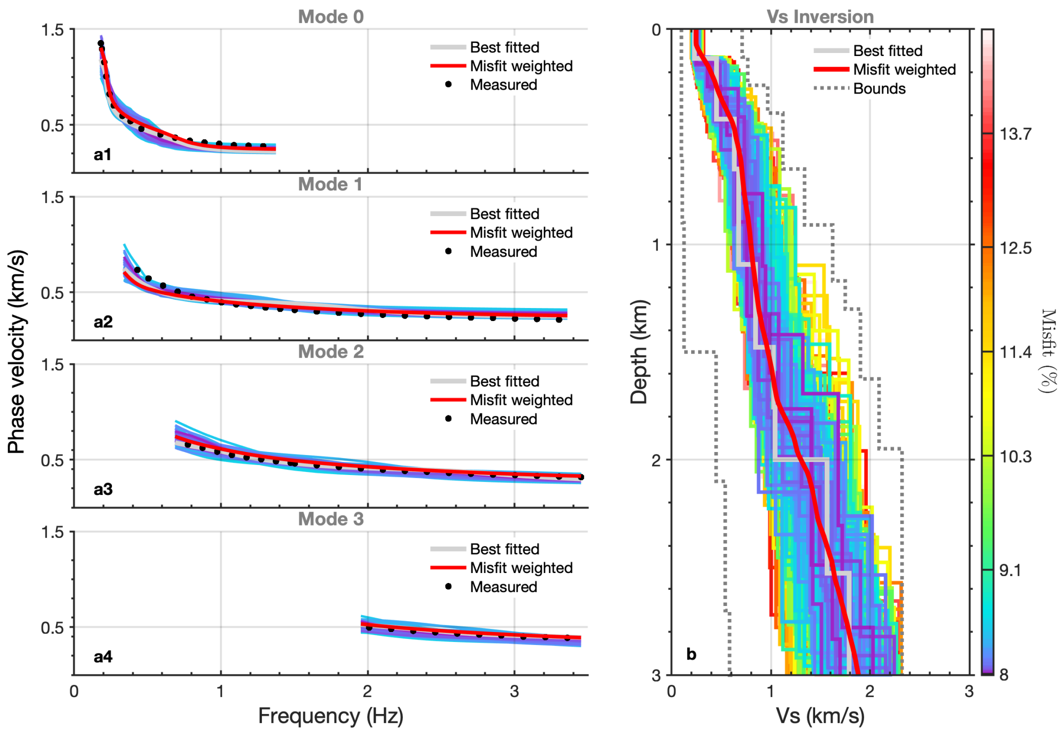

Figure 7. DAS-based multiple-mode surface wave dispersion inversion. (a) shows the measured (the black dotted curves) and the best 400 forwarded (the colored curves) dispersion curves; the gray curves show the the dispersion curve forwarded from the best-fitting model; the red curves depict the dispersion curve forward modelled from the misfit-weighted mean model. (b) presents the best 400 V_s models; the gray and red curves indicate the best fitted model and the misfit-weighted median model; the gray dashed lines indicate the upper and bottom velocity boundaries. Colors in (a) and (b) are coded by misfits as shown on the color map.

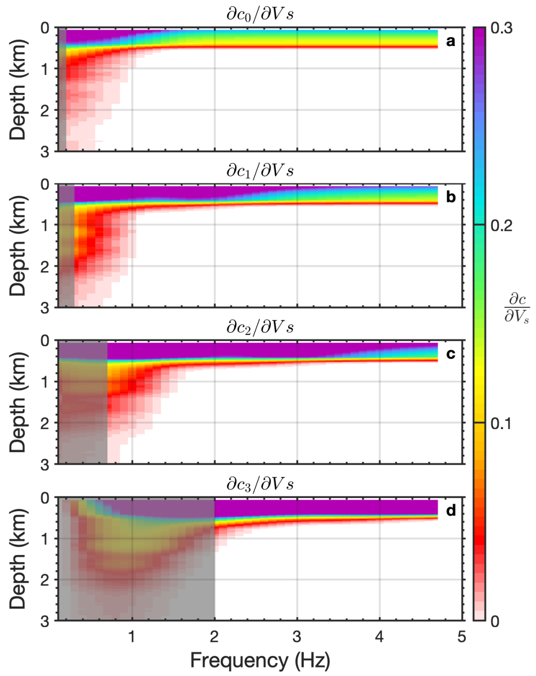

Figure 8. Sensitivity kernel of fundamental (a), first higher mode (b), second higher mode (c) and third higher mode (d) surface waves, respectively. The gray zone indicates the frequency band that could not be reliably identified in the DAS dispersion analysis.

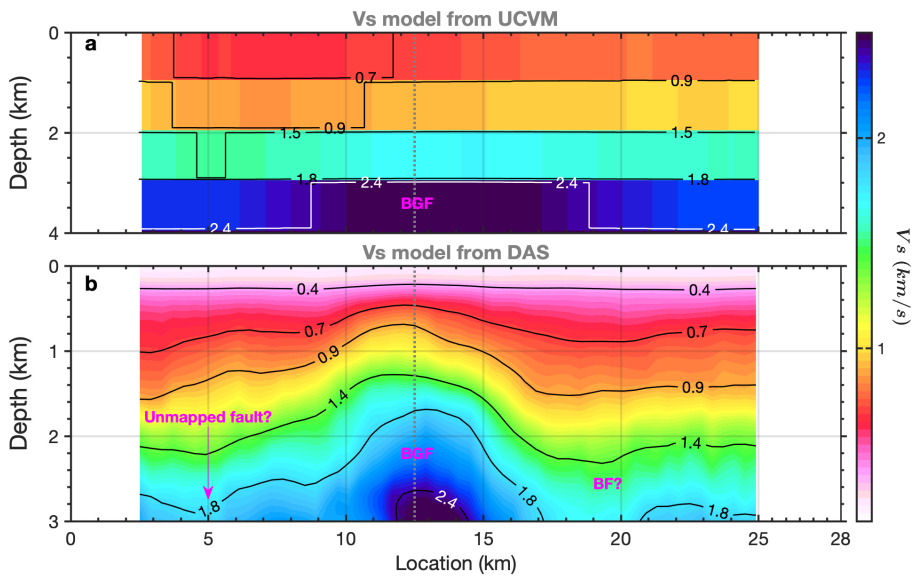

Figure 9. V_s imaging of Brawley geothermal reservoir and Brawley fault. (a) Reference V_s model from IVLSU. (b) Inverted V_s model from DAS ambient noise data. The gray dashed line indicates the location of the model used for comparison in Fig.11a.

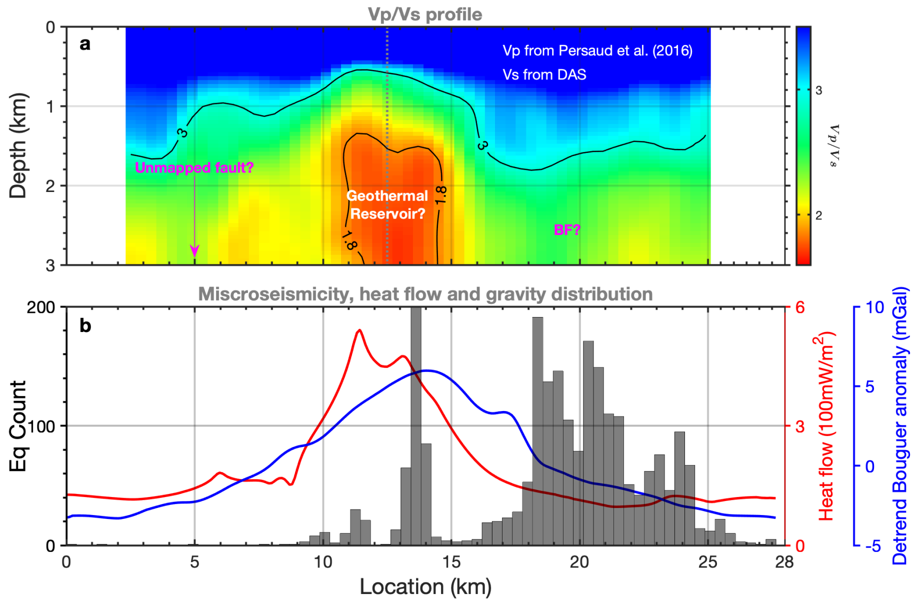

Figure 10. Seismic imaging of Brawley geothermal reservoir and Brawley fault. (a) V_p/V_s profile based on V_p from Persaud et al. (2016) and V_s from DAS. The gray dashed line indicates the location of the model used for comparison in Fig.11a. (b) Distribution of miscroseismicity, heat flow and detrended Bouguer gravity anomaly along the ∼28 km fiber-optic cable. For better visualization, the linear trend of the bouguer gravity has been removed.

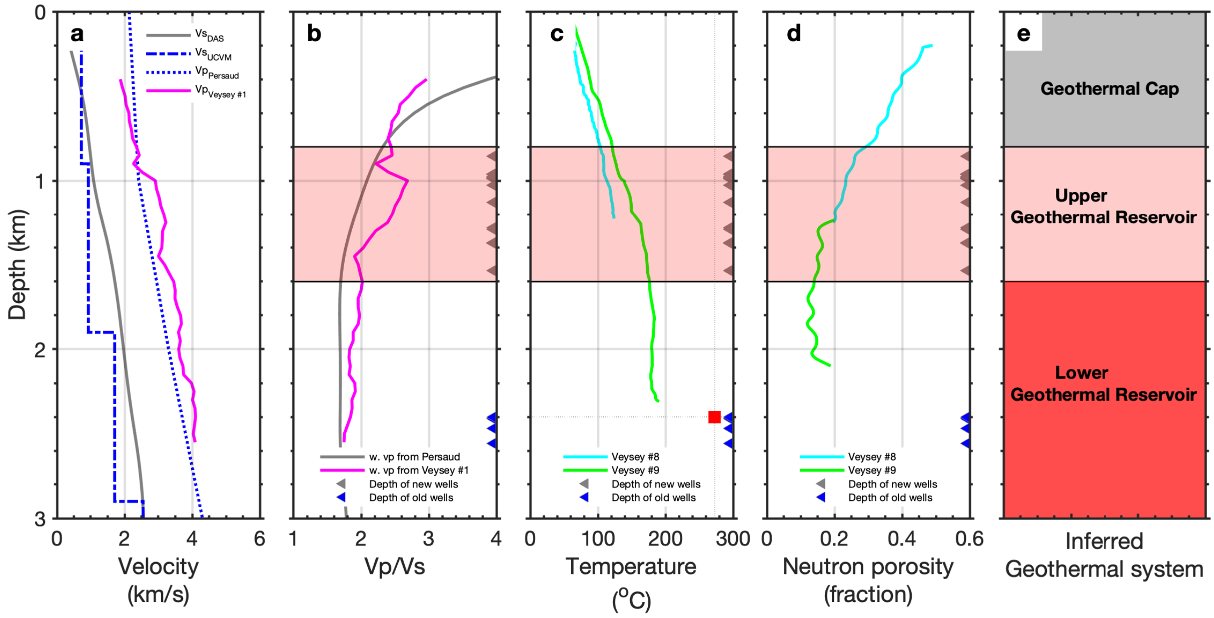

Figure 11. Velocity models, borehole observations and the inferred geothermal system. (a) Velocity models at location 12.5 km (highlighted by the gray dashed line in Fig.9 and Fig.10). V_s model from DAS (the gray solid line) and IVLSU model (the blue dotted-dashed line), V_p model from Persaud et al. (2016) (the blue dotted line) and geothermal well Veysey #1 (the magenta solid line). (b) V_p/V_s profile at location 12.5 km with V_s from DAS and V_p from Persaud et al. (2016) (the gray dotted line) and geothermal well Veysey #1 (the magenta solid line). (c) and (d) show the temperature and neutron porosity observations from geothermal wells, Veysey #8 (the cyan line) and Veysey #9 (the green line), respectively. (e) The inferred geothermal system. The gray triangles indicate the depths of the new production wells developed by Ormat Nevada Inc; the blue triangles indicate the depths of the older production wells developed by Unocal. The red square in c shows the temperature record observed in old geothermal well of Unocal.